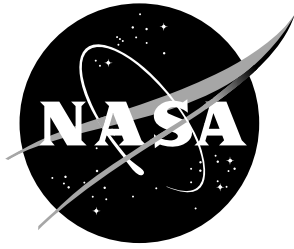


NASA/TM-2020-5000766



VULCAN-CFD Theory Manual: Ver. 7.1.0

*Robert A. Baurle, Jeffery A. White, Tomasz G. Drozda, and Andrew T. Norris
NASA Langley Research Center, Hampton, Virginia*

April 2020

NASA STI Program...in Profile

Since its founding, NASA has been dedicated to the advancement of aeronautics and space science. The NASA scientific and technical information (STI) program plays a key part in helping NASA maintain this important role.

The NASA STI Program operates under the auspices of the Agency Chief Information Officer. It collects, organizes, provides for archiving, and disseminates NASA's STI. The NASA STI Program provides access to the NASA Aeronautics and Space Database and its public interface, the NASA Technical Report Server, thus providing one of the largest collection of aeronautical and space science STI in the world. Results are published in both non-NASA channels and by NASA in the NASA STI Report Series, which includes the following report types:

- **TECHNICAL PUBLICATION.** Reports of completed research or a major significant phase of research that present the results of NASA programs and include extensive data or theoretical analysis. Includes compilations of significant scientific and technical data and information deemed to be of continuing reference value. NASA counterpart of peer-reviewed formal professional papers, but having less stringent limitations on manuscript length and extent of graphic presentations.
- **TECHNICAL MEMORANDUM.** Scientific and technical findings that are preliminary or of specialized interest, e.g., quick release reports, working papers, and bibliographies that contain minimal annotation. Does not contain extensive analysis.
- **CONTRACTOR REPORT.** Scientific and technical findings by NASA-sponsored contractors and grantees.

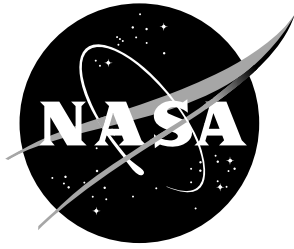
- **CONFERENCE PUBLICATION.** Collected papers from scientific and technical conferences, symposia, seminars, or other meetings sponsored or co-sponsored by NASA.
- **SPECIAL PUBLICATION.** Scientific, technical, or historical information from NASA programs, projects, and missions, often concerned with subjects having substantial public interest.
- **TECHNICAL TRANSLATION.** English-language translations of foreign scientific and technical material pertinent to NASA's mission.

Specialized services also include organizing and publishing research results, distributing specialized research announcements and feeds, providing information desk and personal search support, and enabling data exchange services.

For more information about the NASA STI Program, see the following:

- Access the NASA STI program home page at <http://www.sti.nasa.gov>
- E-mail your question to help@sti.nasa.gov
- Phone the NASA STI Information Desk at 757-864-9658
- Write to:
NASA STI Information Desk
Mail Stop 148
NASA Langley Research Center
Hampton, VA 23681-2199

NASA/TM-2020-5000766



VULCAN-CFD Theory Manual: Ver. 7.1.0

Robert A. Baurle, Jeffery A. White, Tomasz G. Drozda, and Andrew T. Norris
NASA Langley Research Center, Hampton, Virginia

National Aeronautics and
Space Administration

Langley Research Center
Hampton, Virginia 23681-2199

April 2020

The use of trademarks or names of manufacturers in this report is for accurate reporting and does not constitute an official endorsement, either expressed or implied, of such products or manufacturers by the National Aeronautics and Space Administration.

Available from:

NASA STI Program / Mail Stop 148
NASA Langley Research Center
Hampton, VA 23681-2199
Fax: 757-864-6500

Contents

1	Introduction	1
2	Governing Equations	1
2.1	Thermodynamic Nonequilibrium	3
3	Reynolds-Averaged Equations	6
4	Spatially-Filtered Equations	11
5	Hybrid RAS/LES Closures	14
6	Boundary Layer Bleed Models	16
7	Performance Extraction Methods	18
A	Thermodynamic Properties	26
B	Transport Properties	28
C	Finite Rate Chemistry Extensions	30
D	Reynolds-Averaged Turbulence Closure Models	32
D.1	Spalart Allmaras One-Equation Model	32
D.2	Menter k - ω Models	33
D.3	Wilcox 1998 k - ω Model	35
D.4	Wilcox 2006 k - ω Model	36
D.5	Gatski and Rumsey 2003 k - ω EAS Model	38
D.6	Wall Functions	40
D.7	Compressibility Corrections	43
E	Spatially-Filtered Turbulence Closure Models	44
E.1	Smagorinsky Model	44
E.2	Vreman Model	44
E.3	Yoshizawa Model	45
E.4	Dynamic SGS Closures	46
F	Blended RAS/LES Formulation	48
G	Improved Delayed Detached Eddy Simulation	49
H	Bleed Models	51
H.1	Doerffer/Bohning Model	51
H.2	Slater Model	53

I	Conserved Flux Method Data Reduction	56
I.1	CMME Method Data Reduction Details	56
I.2	CMES Method Data Reduction Details	58

1 Introduction

VULCAN-CFD offers a comprehensive set of capabilities to enable the simulation of continuum flowfields from subsonic to hypersonic conditions. The governing equations that are employed include allowances for both chemical and thermal nonequilibrium processes, coupled with a wide variety of turbulence models for both Reynolds-averaged and large eddy simulations. A description of the physical and numerical models available in the software are presented in this document. However, it is emphasized that the descriptions provided are not intended to fully document every aspect of the models employed. Instead, the governing equations, and the models required to simulate them numerically, are presented with the goal of providing a sufficient level of detail to understand their strengths and limitations. The reader is encouraged to access the references provided throughout this document for a more complete explanation of the formulations presented.

2 Governing Equations

The fundamental conservation equations employed by VULCAN-CFD to describe thermally-equilibrated chemically-reacting flows are the Navier-Stokes equations coupled with mass continuity equations for the chemical species. These partial differential equations can be written as

$$\begin{aligned}\frac{\partial \rho}{\partial t} + \frac{\partial}{\partial x_j} (\rho u_j) &= 0 \\ \frac{\partial \rho u_i}{\partial t} + \frac{\partial}{\partial x_j} (\rho u_i u_j) + \frac{\partial}{\partial x_j} (\delta_{ij} P - \tau_{ij}) &= 0 \\ \frac{\partial \rho E}{\partial t} + \frac{\partial}{\partial x_j} (\rho H u_j) + \frac{\partial}{\partial x_j} (q_j - \tau_{ij} u_i) &= 0 \\ \frac{\partial \rho Y_m}{\partial t} + \frac{\partial}{\partial x_j} (\rho Y_m u_j) + \frac{\partial}{\partial x_j} (\rho Y_m V_j^{(m)}) &= \dot{w}_m\end{aligned}\quad (1)$$

where ρ is the density, u_i is the velocity, P is the pressure, E is the total energy, H is the total enthalpy, τ_{ij} is the stress tensor, q_j is the heat flux vector, and Y_m , $V_j^{(m)}$, and \dot{w}_m are the mass fraction, diffusion velocity, and production rate, respectively, of species “ m ”.

The total energy is the sum of the internal and kinetic energy, i.e.,

$$E = e + \frac{1}{2} u_i u_i \quad (2)$$

and the total enthalpy is given by the expression shown below.

$$H = E + \frac{P}{\rho} = h + \frac{1}{2} u_i u_i \quad (3)$$

Here, the mixture enthalpy, h , is defined through the relationship

$$h = \sum_{m=1}^{ns} Y_m h_m \quad (4)$$

with the enthalpy of each species evaluated from a polynomial curve fit as described in Appendix A.

VULCAN-CFD is currently limited to Newtonian fluids, where the stress tensor is related to the strain rate through the following constitutive relation,

$$\tau_{ij} = \mu \left(2S_{ij} - \frac{2}{3} \delta_{ij} S_{kk} \right), \quad S_{ij} = \frac{1}{2} \left(\frac{\partial u_i}{\partial x_j} + \frac{\partial u_j}{\partial x_i} \right) \quad (5)$$

and the heat flux vector (which contains contributions from heat conduction and the energy flux due to interdiffusion processes) is given by the expression provided below.

$$q_j = -\lambda \frac{\partial T}{\partial x_j} + \rho \sum_{m=1}^{ns} h_m Y_m V_j^{(m)} \quad (6)$$

The diffusion velocity of species “ m ” is provided by Fick’s law of diffusion, i.e.,

$$V_j^{(m)} = -\frac{D}{Y_m} \frac{\partial Y_m}{\partial x_j} \quad (7)$$

and the evaluation of the mixture transport properties (μ , λ , and D) is described in Appendix B.

The species production rates are governed by the law of mass action. If a general reaction is denoted by



where ν'_{ml} is the stoichiometric coefficient of reactant “ m ” in reaction “ l ”, ν''_{ml} is the stoichiometric coefficient of product “ m ” in reaction “ l ”, and C_m is the symbol for constituent “ m ” (the $ns + 1$ constituent represents the third body species), then the production rate of species “ m ” can be written in the form shown below.

$$\dot{w}_m = W_m \sum_{l=1}^{nr} (\nu''_{ml} - \nu'_{ml}) \left[k_{f_l} \prod_{n=1}^{ns+1} \left(\frac{\rho_n}{W_n} \right)^{\nu'_{nl}} - k_{b_l} \prod_{n=1}^{ns+1} \left(\frac{\rho_n}{W_n} \right)^{\nu''_{nl}} \right], \quad m = 1, ns \quad (9)$$

Here, k_{f_l} and k_{b_l} are the forward and backward reaction rate coefficients of reaction “ l ”, ρ_n is the product of density and the mass fraction of species “ n ”, and W_m is the molecular weight of species “ m ”. The molar concentration of the third body constituent, M , is defined by

$$\frac{\rho_{ns+1}}{W_{ns+1}} = \sum_{m=1}^{ns} tbe_m \frac{\rho_m}{W_m} \quad (10)$$

where tbe_m is the third body efficiency given by the kinetic model.

The forward reaction rate coefficient is evaluated using the Arrhenius expression,

$$k_{f_l} = A_l T^{b_l} \exp\left(\frac{-T_{a_l}}{T}\right) \quad (11)$$

which mimics the form of the reaction rate derived from kinetic theory. The product $A_i T^{b_i}$ is designed to take into account the frequency of collisions between molecules, and the steric factor associated with the orientation of the colliding molecules. The exponential term is the Boltzmann factor, which represents the fraction of collisions that have an energy greater than the activation energy (defined as the product of the universal gas constant and the activation temperature, T_{a_i}).

The backward reaction rate coefficient can be written in a similar fashion, or obtained from the equilibrium constant through the relationship

$$K_{c_i} = \frac{k_{f_i}}{k_{b_i}} \quad (12)$$

and the equilibrium constant (in terms of molar concentrations) is given by

$$K_{c_i} = (R'_u T)^{-\Delta n_i} \exp\left(\frac{-\Delta G_i}{R_u T}\right) \quad (13)$$

where R_u is the universal gas constant [$J/(molK)$], R'_u is the universal gas constant with units of [$\frac{J \cdot atm}{Kg \cdot mol \cdot K}$], Δn_i is the change in moles from products to reactants, and ΔG_i is the Gibbs energy of reaction defined by the following expression.

$$\Delta G_i = \sum_{m=1}^{ns} (v''_{ml} - v'_{ml}) (W_m g_m) \quad (14)$$

The sensible Gibbs free energy of each species is evaluated from a polynomial curve fit (see Appendix A). VULCAN-CFD can also handle more complex reaction rate representations such as pressure-dependent and arbitrary reaction order kinetics. These extensions are described in Appendix C.

To close the system, an equation of state is needed to relate the thermodynamic properties. At conditions representative of combustion applications (i.e., relatively high temperatures and low pressures), the fluid can be treated as a mixture of perfect gases. Hence, the pressure can be evaluated using the following state equation

$$P = \rho RT \quad (15)$$

where R is the mixture gas constant given by the expression below.

$$R = R_u \sum_{m=1}^{ns} \frac{Y_m}{W_m} \quad (16)$$

2.1 Thermodynamic Nonequilibrium

Flows that are not thermally equilibrated (i.e., the distribution of energy between translational, rotational, vibrational, and electronic modes cannot be described by a single temperature), require the introduction of additional transport equations for those energy modes that are not equilibrated with the translational energy. The cost of solving these additional equations, together with the limited availability of physical constants that describe the finite

rate processes associated with the transfer of energy amongst the various modes, are important factors that must be considered when developing engineering tools for these flows. Historically, the development of the VULCAN-CFD code has been driven by the needs of the scramjet community, which often involves the use of complicated polyatomic molecules (e.g., heavy hydrocarbons) or even JP fuels that are basically “hydrocarbon soups” with an unspecified molecular distribution that simply satisfy certain specified combustion properties. This reality, together with the understanding that most scramjet applications are bounded below Mach 10-12 flight, led to the implementation of a simple two-temperature thermal nonequilibrium model.¹ This formulation assumes that the translation and rotational energy modes are equilibrated at a single temperature T_{tr} , while the vibrational and electronic energy modes are equilibrated at temperature T_{ve} .

The transport equation for the equilibrated vibrational/electronic energy, e_{ve} , is provided by the expression below.

$$\underbrace{\frac{\partial}{\partial t}(\rho e_{ve})}_1 + \underbrace{\frac{\partial}{\partial x_j}(\rho e_{ve} u_j)}_2 = -\underbrace{\frac{\partial q_{ve_j}}{\partial x_j}}_3 + \underbrace{\sum_{m=1}^{nm} \rho_m \left(\frac{e_{ve,m}^* - e_{ve,m}}{\tau_m} \right)}_4 + \underbrace{\sum_{m=1}^{nm} \dot{w}_m \hat{D}_m}_5 - \underbrace{p_e \frac{\partial u_j}{\partial x_j}}_6 + \underbrace{2 \rho_e \frac{3}{2} (T_{tr} - T_{ve}) \sum_{m=1}^{ns} \frac{v_{e,m}}{W_m}}_7 - \underbrace{\sum_{m=1}^{ni} \dot{n}_{e,m} \hat{I}_m}_8 - \underbrace{Q_{rad}}_9 \quad (17)$$

Term (1) represents the time rate of change of the vibrational/electronic energy, e_{ve} . Term (2) accounts for the convection of e_{ve} . Term (3) contains the molecular diffusion processes of the vibrational/electronic energy. Term (4) represents the energy exchange between the vibrational and translational modes due to molecular collisions. Term (5) represents the vibrational energy that is lost (or gained) due to the molecular depletion (dissociation) or production (recombination) that result from chemical kinetics. Term (6) is a term that accounts for the combined effect of the convection of electron pressure and the work done on electrons by the electric field induced by the electron pressure gradient. Term (7) accounts for the energy exchange due to elastic collisions between free electrons and atoms/molecules. Term (8) represents the electronic energy loss due to electron impact ionization. Finally, Term (9) accounts for the loss of electronic energy due to radiation caused by electronic transitions. Terms (6) - (8) are nonzero only when free electrons are present. These terms are currently not accounted for in VULCAN-CFD, due in part to a lack of sources for the species data required to evaluate these terms. As a result, the current thermal nonequilibrium formulation should not be used for problems where significant ionization is present. The radiant energy transfer rate due to electronic transitions (Q_{rad}) is also neglected in VULCAN-CFD.

The vibrational/electronic heat flux vector, q_{ve_j} , accounts for both heat conduction due to vibrational/electronic temperature gradients and the transfer of vibrational/electronic enthalpy due to gradients in species composition with Fick’s law of diffusion used to model this latter effect.

$$q_{ve_j} = -\lambda_{ve} \frac{\partial T_{ve}}{\partial x_j} - \rho \sum_{m=1}^{ns} h_{ve,m} Y_m V_j^{(m)} \quad (18)$$

The assumptions used above to model q_{vej} are consistent with how VULCAN-CFD models the heat flux vector for thermally-equilibrated flows.

The Landau-Teller vibrational/translational energy relaxation process is modeled as

$$\sum_{m=1}^{nm} \rho_m \left(\frac{e_{ve,m}^* - e_{ve,m}}{\tau_m} \right) = \sum_{m=1}^{nm} \rho_m \left(\frac{e_{ve,m}(T_{tr}) - e_{ve,m}(T_{ve})}{\tau_m} \right) \quad (19)$$

where nm is the number of vibrational modes (summed over all molecules), and τ_m is the relaxation time of vibrational mode “ m ”. VULCAN-CFD computes this relaxation time as a blend of two functional forms. The first is the generalized form of the semiempirical correlation developed by Millikan and White²

$$\tau_m \approx \frac{\sum_{n=1}^{ns} \frac{Y_n}{W_n}}{p \sum_{n=1}^{ns} \frac{Y_n}{W_n} \left(\exp \left[A_{mn} \left(T_{tr}^{-\frac{1}{3}} - B_{mn} \right) - 18.42 \right] \right)^{-1}} \quad (20)$$

where the pressure, p , has units of atm. The coefficients A_{mn} and B_{mn} are by default given by the following formulas²

$$\begin{aligned} A_{mn} &= 1.16 \times 10^{-3} \mu_{mn}^{\frac{1}{2}} \theta_{v,m}^{\frac{4}{3}} \\ B_{mn} &= 0.015 \mu_{mn}^{\frac{1}{4}} \end{aligned} \quad (21)$$

where $\theta_{v,m}$ is the characteristic vibrational mode temperature of mode “ m ”, and μ_{mn} is the reduced molecular weight between species “ n ” and the molecule associated with mode “ m ”.

$$\mu_m = \frac{W_m W_n}{W_m + W_n} \quad (22)$$

The Millikan and White formula tends to be reasonably accurate for temperatures up to approximately 5000 K. At higher temperatures, this correlation tends to underestimate measured relaxation times, and Park’s^{3,4} expression for the vibrational relaxation time (shown below) is often preferred.

$$\tau_m \approx (\sigma_m \bar{c}_m n)^{-1} \quad (23)$$

Here, σ_m is the effective cross section (given in units of m^2) for vibrational relaxation,³ \bar{c}_m is the average velocity of the molecule corresponding to mode “ m ”, and n is the mixture number density. These properties are obtained from the expressions below

$$\sigma_m = 3.0 \times 10^{-21} \left(\frac{50,000}{T_{tr}} \right) \quad (24)$$

$$\bar{c}_m = \left(\frac{8 R_u T_{tr}}{\pi W_m} \right)^{\frac{1}{2}} \quad (25)$$

$$n = \rho N_A \sum_{n=1}^{ns} \frac{Y_n}{W_n} \quad (26)$$

where N_A is the Avogadro constant. The final blended relaxation time used in Eq. 19 is simply the sum of the Millikan & White and Park functional forms.

The creation (or destruction) of vibrational energy due to chemical reactions is modeled as

$$\sum_{m=1}^{nm} \dot{w}_m \hat{D}_m \approx \sum_{m=1}^{nm} \dot{w}_m (C_{pd} e_{ve,m}) \quad (27)$$

where \hat{D}_m denotes the vibrational energy per unit mass of the molecule associated with vibrational mode “ m ” that is created or destroyed at rate \dot{w}_m . The model used in Eq. 27 is based on the concept of preferential dissociation, which assumes that a molecule is more likely to dissociate if it is in a higher vibrational state (or conversely, atoms that recombine are more likely to create molecules in a higher vibrational state). This implies that \hat{D}_m should be larger than the average vibrational energy of the system. A value of C_{pd} greater than unity produces the preferential dissociation effect where molecules in a higher vibrational state are “preferentially” dissociated as compared to those in a lower vibrational state.

The evaluation of finite rate chemical kinetics introduces complications when the gas is not thermally equilibrated. In particular, the time scale associated with dissociative chemical reactions is often comparable to the characteristic time associated with vibrational relaxation. This condition implies a potential coupling between the vibrational and chemical finite rate processes. VULCAN-CFD utilizes the Park^{3,5} formulation to empirically model this effect. The Park concept assumes that an appropriately weighted combination of the translational/rotational and vibrational/electronic temperatures, i.e.,

$$T^* = T_{tr}^\alpha T_{ve}^{1-\alpha}, \quad 0.5 \leq \alpha \leq 0.7 \quad (28)$$

can be used to characterize the reaction rate of dissociation reactions, while all other chemical reaction classes (recombination, exchange, etc.) are assumed to be characterized by the translational/rotational temperature.

3 Reynolds-Averaged Equations

The grid density required to resolve all of the relevant turbulent length scales prohibit a direct numerical solution of the Navier-Stokes equations at high Reynolds numbers typical of most applications of engineering interest. Instead, a more cost effective strategy is to work with the time-averaged governing equations, which forms the basis of Reynolds-Averaged Simulations (RAS). All details of the turbulent flowfield structure are lost in the time averaging process, however, the information desired from a simulation is more often than not limited to time-averaged properties. Thus, the time (or Reynolds) averaged equations are usually sufficient provided that adequate models are chosen to close the resulting equation set.

There are two types of variable decomposition methods that are frequently used to average the compressible flow equations. The first is the conventional time-averaged decomposition, which for a random variable ϕ , is defined as

$$\phi = \bar{\phi} + \phi', \quad \bar{\phi} \equiv \lim_{\Delta t \rightarrow \infty} \frac{1}{\Delta t} \int_{t_0}^{t_0 + \Delta t} \phi dt \quad (29)$$

and the second method is the Favré (or mass weighted) decomposition, which is convenient for correlations involving the density.

$$\phi = \tilde{\phi} + \phi'', \quad \tilde{\phi} \equiv \frac{1}{\bar{\rho}} \lim_{\Delta t \rightarrow \infty} \frac{1}{\Delta t} \int_{t_o}^{t_o + \Delta t} \rho \phi dt \quad (30)$$

VULCAN-CFD employs a combination of the above decomposition procedures as shown below.

$$\begin{aligned} \rho &= \bar{\rho} + \rho' & u_i &= \tilde{u}_i + u_i'' & P &= \bar{P} + P' \\ \tau_{ij} &= \bar{\tau}_{ij} + \tau'_{ij} & E &= \tilde{E} + E'' & H &= \tilde{H} + H'' \\ q_i &= \bar{q}_i + q'_i & Y_m &= \tilde{Y}_m + Y_m'' & \dot{w}_m &= \bar{\dot{w}}_m + \dot{w}'_m \\ & & e_{ve} &= \tilde{e}_{ve} + e_{ve}'' \end{aligned} \quad (31)$$

Substituting the decomposed variables into the governing equations and averaging the result yields the Reynolds-averaged equation set, i.e.,

$$\begin{aligned} \frac{\partial \bar{\rho}}{\partial t} + \frac{\partial}{\partial x_j} (\bar{\rho} \tilde{u}_j) &= 0 \\ \frac{\partial}{\partial t} (\bar{\rho} \tilde{u}_i) + \frac{\partial}{\partial x_j} (\bar{\rho} \tilde{u}_i \tilde{u}_j + \bar{\rho} \widetilde{u_i'' u_j''}) + \frac{\partial}{\partial x_j} (\delta_{ij} \bar{P} - \bar{\tau}_{ij}) &= 0 \\ \frac{\partial}{\partial t} (\bar{\rho} \tilde{E}) + \frac{\partial}{\partial x_j} (\bar{\rho} \tilde{H} \tilde{u}_j + \bar{\rho} \widetilde{H'' u_j''}) + \frac{\partial}{\partial x_j} (\bar{q}_j - \bar{\tau}_{ij} \tilde{u}_i - \overline{\tau_{ij} u_i''}) &= 0 \\ \frac{\partial}{\partial t} (\bar{\rho} \tilde{Y}_m) + \frac{\partial}{\partial x_j} (\bar{\rho} \tilde{Y}_m \tilde{u}_j + \bar{\rho} \widetilde{Y_m'' u_j''}) + \frac{\partial}{\partial x_j} (\bar{\rho} \tilde{Y}_m \tilde{V}_j^{(m)} + \overline{\rho Y_m'' V_j^{(m)''}}) &= \bar{\dot{w}}_m \end{aligned} \quad (32)$$

and for flows in thermal nonequilibrium, the Reynolds-averaged vibrational/electronic energy equation utilized in VULCAN-CFD is provided by the equation below.

$$\frac{\partial}{\partial t} (\bar{\rho} \tilde{e}_{ve}) + \frac{\partial}{\partial x_j} (\bar{\rho} \tilde{e}_{ve} \tilde{u}_j + \bar{\rho} \widetilde{e_{ve}'' u_j''}) = -\frac{\partial \bar{q}_{ve,j}}{\partial x_j} + \sum_{m=1}^{nm} \overline{\rho_m \left(\frac{e_{ve,m}^* - e_{ve,m}}{\tau_m} \right)} + \sum_{m=1}^{nm} \bar{\dot{w}}_m \hat{D}_m \quad (33)$$

The averaging process has introduced several higher-order correlations, which must be modeled. The first is the Reynolds stress tensor ($\bar{\rho} \widetilde{u_i'' u_j''}$), which is typically modeled using the Boussinesq approximation.

$$\bar{\rho} \widetilde{u_i'' u_j''} = \frac{2}{3} \delta_{ij} \bar{\rho} \tilde{k} - \mu_t \left(2\tilde{S}_{ij} - \frac{2}{3} \delta_{ij} \tilde{S}_{kk} \right) \quad (34)$$

In the above expression, \tilde{k} is the turbulent kinetic energy defined by

$$\tilde{k} \equiv \frac{1}{2} \widetilde{u_i'' u_i''} \quad (35)$$

and μ_t is the eddy viscosity. The eddy viscosity is dependent on the properties of the turbulent flow. This is in contrast to the molecular viscosity, which is a transport property of the fluid. The eddy viscosity models available in VULCAN-CFD are described in Appendix D.

The time-averaged pressure is obtained from the perfect gas expression by neglecting the impact of composition fluctuations on the mixture molecular weight, i.e.,

$$\bar{P} = \overline{\rho RT} \approx \bar{\rho} R \tilde{T}, \quad R = R_u \sum_{m=1}^{ns} \frac{\tilde{Y}_m}{W_m} \quad (36)$$

and the time-averaged molecular stress tensor is approximated by evaluating the mixture molecular viscosity based solely on mean values of temperature and composition, and neglecting differences between the time-averaged and Favré-averaged velocity components.

$$\bar{\tau}_{ij} = \mu \left(\frac{\partial u_i}{\partial x_j} + \frac{\partial u_j}{\partial x_i} \right) - \frac{2}{3} \delta_{ij} \mu \frac{\partial u_k}{\partial x_k} \approx \mu \left(\frac{\partial \tilde{u}_i}{\partial x_j} + \frac{\partial \tilde{u}_j}{\partial x_i} \right) - \frac{2}{3} \delta_{ij} \mu \frac{\partial \tilde{u}_k}{\partial x_k} \quad (37)$$

These assumptions are valid very close to solid surfaces where the flow is pseudolaminar. In these regions, the effects of turbulent fluctuations are small, and the time averages and Favré averages are approximately equal. In fully turbulent regions, the assumptions made here are less consequential, since the Reynolds stress tensor tends to dominate the molecular stress tensor. Direct numerical simulation (DNS) data⁶ have given further support for approximations of this type.

Using the definition of the turbulent kinetic energy, the Favré-averaged total energy and enthalpy can be written as shown below.

$$\begin{aligned} \tilde{E} &= \tilde{e} + \frac{1}{2} (\tilde{u}_i \tilde{u}_i + 2\tilde{k}) \\ \tilde{H} &= \tilde{h} + \frac{1}{2} (\tilde{u}_i \tilde{u}_i + 2\tilde{k}) \end{aligned} \quad (38)$$

An expression for the Favré fluctuating component of the total enthalpy is obtained by subtracting the mean total enthalpy from the instantaneous value as illustrated below.

$$H'' = h'' + \tilde{u}_i u_i'' + \frac{1}{2} (u_i'' u_i'' - 2\tilde{k}) \quad (39)$$

Given this expression, the correlation $\bar{\rho} \widetilde{H'' u_j''}$ can be expanded to yield the following relationship for $\bar{\rho} \widetilde{H'' u_j''}$.

$$\bar{\rho} \widetilde{H'' u_j''} = \bar{\rho} \widetilde{h'' u_j''} + \bar{\rho} \widetilde{\tilde{u}_i u_i'' u_j''} + \bar{\rho} \widetilde{k u_j''} \quad (40)$$

The first term is the Reynolds heat flux vector, which is modeled using the gradient diffusion approximation, i.e.,

$$\bar{\rho} \widetilde{h'' u_j''} = -\frac{\mu_t}{Pr_t} \frac{\partial \tilde{h}}{\partial x_j} \quad (41)$$

where Pr_t is the turbulent Prandtl number. The second term is the dot product of the mean velocity with the Reynolds stress tensor (which was modeled previously). The third term represents the turbulent transport of the turbulent kinetic energy. The gradient diffusion approximation is also used to model this term,

$$\bar{\rho} \widetilde{k u_j''} = -\frac{\mu_t}{\sigma_k} \frac{\partial \tilde{k}}{\partial x_j} \quad (42)$$

where σ_k is a closure coefficient that varies depending on the turbulence model employed. The next term to be modeled is a molecular diffusion term. For incompressible flows, this term is well approximated by the following expression,

$$\frac{\partial}{\partial x_j} \left(\overline{\tau_{ij} u_i''} \right) \approx \frac{\partial}{\partial x_j} \left(\mu \frac{\partial \tilde{k}}{\partial x_j} \right) \quad (43)$$

and for compressible flows, it is assumed that the above relation is still a reasonable approximation.

As with the evaluation of the mean molecular stress tensor, the time average of the heat flux vector is evaluated by replacing time-averaged quantities with Favré-averaged quantities, and ignoring the effects of temperature and composition fluctuations on the molecular transport coefficients. If the effect of temperature fluctuations on the species enthalpies are also neglected, then the mean heat flux vector is obtained from the following expression.

$$\bar{q}_j = -\lambda \frac{\partial \tilde{T}}{\partial x_j} - \bar{\rho} D \sum_{m=1}^{ns} h_m(\tilde{T}) \frac{\partial \tilde{Y}_m}{\partial x_j} \quad (44)$$

An analogous set of assumptions is applied to the heat flux vectors for flows in thermodynamic nonequilibrium.

$$\begin{aligned} \bar{q}_j &= -\lambda_{tr} \frac{\partial \tilde{T}_{tr}}{\partial x_j} - \lambda_{ve} \frac{\partial \tilde{T}_{ve}}{\partial x_j} - \bar{\rho} D \sum_{m=1}^{ns} h_m(\tilde{T}_{tr}, \tilde{T}_{ve}) \frac{\partial \tilde{Y}_m}{\partial x_j} \\ \bar{q}_{ve_j} &= -\lambda_{ve} \frac{\partial \tilde{T}_{ve}}{\partial x_j} - \bar{\rho} D \sum_{m=1}^{ns} h_{ve,m}(\tilde{T}_{ve}) \frac{\partial \tilde{Y}_m}{\partial x_j} \end{aligned} \quad (45)$$

The Reynolds mass flux vector, $\bar{\rho} \widetilde{Y_m'' u_j''}$, is modeled via the gradient diffusion approximation

$$\bar{\rho} \widetilde{Y_m'' u_j''} = -\frac{\mu_t}{S c_t} \frac{\partial \tilde{Y}_m}{\partial x_j} \quad (46)$$

where $S c_t$ is the turbulent Schmidt number. The molecular diffusion of mass is approximated by ignoring the effects of turbulent fluctuations on the diffusion coefficient, and neglecting gradients of Favré mass fraction fluctuations.

$$\bar{\rho} \tilde{Y}_m \tilde{V}_j^{(m)} + \overline{\rho Y_m'' V_j^{(m)''}} = \frac{\overline{\rho} \partial \tilde{Y}_m}{\partial x_j} + \overline{\rho D \frac{\partial Y_m''}{\partial x_j}} \approx \bar{\rho} D \frac{\partial \tilde{Y}_m}{\partial x_j} \quad (47)$$

The same approximation used to close the Reynolds heat flux vector is also used to close the Reynolds vibrational/electronic energy flux vector, $\bar{\rho} \widetilde{e_{ve}'' u_j''}$,

$$\bar{\rho} \widetilde{e_{ve}'' u_j''} = -\frac{\mu_t}{Pr_t} \frac{\partial \tilde{e}_{ve}}{\partial x_j} \quad (48)$$

and the time-averaged vibrational/translational energy relaxation source term is approximated by neglecting the effect of temperature fluctuations on the species specific heats, and ignoring the influence of turbulent fluctuations on the relaxation time.

$$\sum_{m=1}^{nm} \overline{\rho_m \left(\frac{e_{ve,m}^* - e_{ve,m}}{\tau_m} \right)} \approx \sum_{m=1}^{nm} \bar{\rho}_m \left(\frac{e_{ve,m}(\tilde{T}_{tr}) - e_{ve,m}(\tilde{T}_{ve})}{\tau_m(\bar{P}, \tilde{T}_{tr}, \tilde{Y}_m)} \right) \quad (49)$$

A Reynolds decomposition of the time-averaged species production rates (\bar{w}_m) yields a preponderance of terms, most of which are unknown higher-order correlations. Thus, there is little hope for developing closure models for all of the individual correlations that are

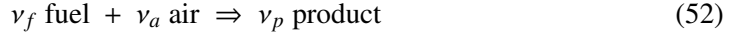
present. Many advanced turbulence-chemistry models have been proposed over the years to close this term,⁷⁻¹⁰ but to date these formulations have not significantly outperformed the laminar chemistry approximation for practical supersonic combustion applications, which can be expressed in the form shown below.

$$\bar{w}_m \approx \dot{w}_m(\bar{T}, \bar{\rho}_m) \quad (50)$$

A laminar approximation is also employed for the chemical source term present in the vibrational/electronic energy equation.

$$\sum_{m=1}^{nm} \overline{\dot{w}_m \hat{D}} \approx \sum_{m=1}^{nm} \dot{w}_m(\bar{T}_{tr}, \bar{T}_{ve}, \bar{\rho}_m) (C_{pd} e_{ve,m}(\bar{T}_{ve})) \quad (51)$$

A rudimentary turbulence-chemistry closure model is available in VULCAN-CFD based on the eddy breakup concept of Magnussen and Hjertager.¹¹ Models based on this concept address the turbulence closure problem by assuming that the rate of reaction is limited by the rate of mixing between fuel and oxygen carrying eddies, rather than on chemical kinetic time scales. In regions of high turbulence levels, the eddy lifetime is short, leading to large eddy dissipation rates and more rapid mixing. Models based on this concept correlate this phenomenon to higher reaction rates. The Magnussen and Hjertager model is applicable to irreversible reactions only, and applies to the following single-reaction step for fuel and air



where the stoichiometric coefficients are related to the constituent molecular weights (W_m) and the stoichiometric air-to-fuel mass ratio, $(air/fuel)_{st}$. The expressions that define the stoichiometric coefficients are provided below.

$$\nu_f = 1.0, \quad \nu_a = \frac{W_f}{W_a} \left(\frac{air}{fuel} \right)_{st}, \quad \nu_p = \frac{W_f}{W_p} \left[\left(\frac{air}{fuel} \right)_{st} + 1.0 \right] \quad (53)$$

Given these definitions, the chemical source term of species “ m ” (where m represents either fuel, air, or product) can be written as

$$\bar{w}_m = \nu_m W_m \frac{A}{\tau_t} \text{MIN} \left[\frac{\bar{\rho}_f}{\nu_f W_f}, \frac{\bar{\rho}_a}{\nu_a W_a}, \frac{B \bar{\rho}_p}{\nu_p W_p} \right] \quad (54)$$

where τ_t is the turbulent time scale (turbulence model specific) and A , B are closure coefficients. The first two terms within the MIN function are intended for nonpremixed combustion regions, where the turbulent eddies mix fuel and air into the reaction zones. The third term in the MIN function is intended for premixed combustion scenarios, where the turbulent eddies mix cold reactants with hot products in the reaction zones. This model is an attractive option from a computational viewpoint, as it offers a quick turnaround time compared with true finite rate models that require the tracking of numerous chemical species. Moreover, the use of a single time scale for chemical reaction (τ_t) alleviates much of the stiffness associated with more complex chemical systems. However, one must be cognizant of the fact that this model correlates chemical processes with turbulent mixing. Consequently, it cannot be used to predict finite rate effects like blowout limits or combustor ignition characteristics.

4 Spatially-Filtered Equations

The development of Reynolds-averaged closures with sufficient accuracy to satisfy the demands of the aerospace industry has proven to be an elusive endeavor. Moreover, numerical simulations are increasingly being utilized for flows that are fundamentally unsteady (e.g., flow control or pulsed fuel injection). For unsteady applications, the use of the Reynolds-averaged equations is dubious unless all unsteady scales of interest are known to be significantly larger than the largest turbulence scales present. A reasonable approach to address either of these scenarios is to consider the spatially-filtered equation set. Spatial filtering relies on the explicit removal of the smallest scales of turbulent motions using a low pass filtering operator, so that only length scales smaller than this value must be modeled. This approach is the basis for Large Eddy Simulations (LES). In LES, the filter width (Δ) is intended to correspond to a length scale within the inertial range of the turbulence spectrum; a choice that typically removes about 20% (or less) of the turbulent kinetic energy.¹² Given that only the smaller scales are removed by filtering, with their energetic content small compared to those resolved numerically, the hope is that any errors incurred in modeling will have a small impact on the resolved turbulence motions. Moreover, the smaller turbulence scales should be less dependent on the specifics of the geometry than the larger scales. As a result, one can reasonably expect that models developed for only the smallest scales of turbulence will be more universal than those developed for the entire range of scales.

The filtering operation involves a convolution integral of the form

$$\bar{\phi} = \int_{-\infty}^{+\infty} \mathcal{G}(x' - x) \phi \, dx' \quad (55)$$

where $\bar{\phi}$ is the filtered value of some quantity ϕ , and $\mathcal{G}(x' - x)$ denotes a filter function with the following properties:

- temporally invariant [$\mathcal{G}(x' - x) \neq f(t)$]
- positive definite [$\mathcal{G}(x' - x) \geq 0$ for all x]
- symmetric [$\mathcal{G}(x' - x) = \mathcal{G}(x - x')$]
- localized [$\mathcal{G}(x' - x) \rightarrow 0$, for $x - x' \gtrsim \Delta/2$]
- constant preserving [$\int_{-\infty}^{+\infty} \mathcal{G}(x' - x) \, dx' = 1$]

A Favré filtered quantity can also be defined in a manner analogous to that used for the Reynolds-averaged equation set, i.e.,

$$\tilde{\phi} = \frac{\overline{\rho\phi}}{\bar{\rho}} \quad (56)$$

to simplify the notation for variable density flows. The application of the filtering operation

to the governing equations results in the following spatially-filtered equation set,

$$\begin{aligned}
\frac{\partial \bar{\rho}}{\partial t} + \frac{\partial}{\partial x_j} (\bar{\rho} \tilde{u}_j) &= 0 \\
\frac{\partial \bar{\rho} \tilde{u}_i}{\partial t} + \frac{\partial}{\partial x_j} (\bar{\rho} \tilde{u}_i \tilde{u}_j + [\bar{\rho} \widetilde{u_i u_j} - \bar{\rho} \tilde{u}_i \tilde{u}_j]) + \frac{\partial}{\partial x_j} (\delta_{ij} \bar{P} - \bar{\tau}_{ij}) &= 0 \\
\frac{\partial \bar{\rho} \tilde{E}}{\partial t} + \frac{\partial}{\partial x_j} (\bar{\rho} \tilde{H} \tilde{u}_j + [\bar{\rho} \widetilde{H u_j} - \bar{\rho} \tilde{H} \tilde{u}_j]) + \frac{\partial}{\partial x_j} (\bar{q}_j - \bar{\tau}_{ij} \tilde{u}_i - [\bar{\tau}_{ij} \overline{u_i} - \bar{\tau}_{ij} \tilde{u}_i]) &= 0 \\
\frac{\partial \bar{\rho} \tilde{Y}_m}{\partial t} + \frac{\partial}{\partial x_j} (\bar{\rho} \tilde{Y}_m \tilde{u}_j + [\bar{\rho} \widetilde{Y_m u_j} - \bar{\rho} \tilde{Y}_m \tilde{u}_j]) + \frac{\partial}{\partial x_j} (\bar{\rho} \tilde{Y}_m \tilde{V}_j^{(m)} + [\bar{\rho} \widetilde{Y_m V_j^{(m)}} - \bar{\rho} \tilde{Y}_m \tilde{V}_j^{(m)}]) &= \bar{w}_m
\end{aligned} \tag{57}$$

and for thermal nonequilibrium flows, the spatially-filtered form of the vibrational/electronic energy equation utilized in VULCAN-CFD is provided by the equation below.

$$\frac{\partial \bar{\rho} \tilde{e}_{ve}}{\partial t} + \frac{\partial}{\partial x_j} (\bar{\rho} \tilde{e}_{ve} \tilde{u}_j + [\bar{\rho} \widetilde{e_{ve} u_j} - \bar{\rho} \tilde{e}_{ve} \tilde{u}_j]) = -\frac{\partial \bar{q}_{ve,j}}{\partial x_j} + \sum_{m=1}^{nm} \overline{\rho_m \left(\frac{e_{ve,m}^* - e_{ve,m}}{\tau_m} \right)} + \sum_{m=1}^{nm} \overline{\dot{w}_m \hat{D}_m} \tag{58}$$

The terms within the square brackets represent the small scale information lost during the filtering operation, and are often referred to as the SubGrid Scale (or SGS) terms. This equation set is structurally similar to the Reynolds-averaged equations (see Eqs. 32 and 33), an observation that also carries over to the closure functions for the SGS terms. For instance, the SGS stress tensor is typically modeled via the Boussinesq relationship

$$[\bar{\rho} \widetilde{u_i u_j} - \bar{\rho} \tilde{u}_i \tilde{u}_j] = \frac{2}{3} \delta_{ij} \bar{\rho} \tilde{k} - \mu_{sgs} \left(2\tilde{S}_{ij} - \frac{2}{3} \delta_{ij} \tilde{S}_{kk} \right) \tag{59}$$

where \tilde{k} is the subgrid turbulent kinetic energy,

$$\tilde{k} \equiv \frac{1}{2} (\overline{u_i u_i} - \tilde{u}_i \tilde{u}_i) \tag{60}$$

and μ_{sgs} is the subgrid viscosity. The subgrid viscosity, like the eddy viscosity for the Reynolds-averaged equations, is intended to dissipate the turbulence energy that is not resolved by the simulation. Hence, the role of the subgrid viscosity is to dissipate only the smallest turbulence scales that are not resolved by the grid. This behavior is realized by defining the subgrid viscosity length scale to be a quantity proportional to the filter width, Δ . The various subgrid viscosity models available in VULCAN-CFD are described in Appendix E.

The Favré-filtered total energy and enthalpy are defined by the following expressions,

$$\begin{aligned}
\tilde{E} &= \tilde{e} + \frac{1}{2} (\tilde{u}_i \tilde{u}_i + 2\tilde{k}) \\
\tilde{H} &= \tilde{h} + \frac{1}{2} (\tilde{u}_i \tilde{u}_i + 2\tilde{k})
\end{aligned} \tag{61}$$

allowing the subgrid term involving the total enthalpy to be decomposed as

$$[\bar{\rho} \widetilde{H u_j} - \bar{\rho} \tilde{H} \tilde{u}_j] = \left[\bar{\rho} \widetilde{h u_j} + \frac{1}{2} \bar{\rho} \widetilde{u_i u_i u_j} - \bar{\rho} \left(\tilde{h} + \frac{1}{2} (\tilde{u}_i \tilde{u}_i + 2\tilde{k}) \right) \tilde{u}_j \right] \tag{62}$$

where the $\overline{\rho u_i \widetilde{u}_i u_j}$ correlation can be further decomposed to the form shown below.

$$\frac{1}{2} \overline{\rho u_i \widetilde{u}_i u_j} = \frac{1}{2} \overline{\rho u_i \widetilde{u}_i} \widetilde{u}_j + \left[\frac{1}{2} \overline{\rho u_i \widetilde{u}_i u_j} - \frac{1}{2} \overline{\rho u_i \widetilde{u}_i} \widetilde{u}_j \right] \quad (63)$$

The subgrid terms that appear in these expressions are modeled via the gradient diffusion approximation, i.e.,

$$\begin{aligned} [\overline{\rho h u_j} - \overline{\rho \tilde{h} u_j}] &= -\frac{\mu_{sgs}}{Pr_{sgs}} \frac{\partial \tilde{h}}{\partial x_j} \\ \left[\frac{1}{2} \overline{\rho u_i \widetilde{u}_i u_j} - \frac{1}{2} \overline{\rho u_i \widetilde{u}_i} \widetilde{u}_j \right] &= -\frac{\mu_{sgs}}{\sigma_k} \frac{\partial \tilde{k}}{\partial x_j} \end{aligned} \quad (64)$$

as are the subgrid mass flux and vibrational/electronic energy flux vectors.

$$\begin{aligned} [\overline{\rho \tilde{Y}_m u_j} - \overline{\rho \tilde{Y}_m} \widetilde{u}_j] &= -\frac{\mu_{sgs}}{Sc_{sgs}} \frac{\partial \tilde{Y}_m}{\partial x_j} \\ [\overline{\rho \tilde{e}_{ve} u_j} - \overline{\rho \tilde{e}_{ve}} \widetilde{u}_j] &= -\frac{\mu_{sgs}}{Pr_{sgs}} \frac{\partial \tilde{e}_{ve}}{\partial x_j} \end{aligned} \quad (65)$$

In the expressions above, Pr_{sgs} and Sc_{sgs} are the subgrid Prandtl and Schmidt numbers, respectively. The species chemical production rates and the source terms in the vibrational/electronic energy equation are closed via a laminar closure assumption.

$$\begin{aligned} \bar{w}_m &\approx \dot{w}_m(\tilde{T}, \bar{\rho}_m) \\ \sum_{m=1}^{nm} \overline{\rho_m \left(\frac{e_{ve,m}^* - e_{ve,m}}{\tau_m} \right)} &\approx \sum_{m=1}^{nm} \bar{\rho}_m \left(\frac{e_{ve,m}(\tilde{T}_{tr}) - e_{ve,m}(\tilde{T}_{ve})}{\tau_m(\bar{P}, \tilde{T}_{tr}, \tilde{Y}_m)} \right) \\ \sum_{m=1}^{nm} \overline{\dot{w}_m \hat{D}} &\approx \sum_{m=1}^{nm} \dot{w}_m(\tilde{T}_{tr}, \tilde{T}_{ve}, \bar{\rho}_m) (C_{pd} e_{ve,m}(\tilde{T}_{ve})) \end{aligned} \quad (66)$$

The closures for the remaining terms are analogous to those used for the Reynolds-averaged equation set.

$$\begin{aligned} \bar{P} &= \overline{\rho RT} \approx \bar{\rho} Ru \sum_{m=1}^{ns} \frac{\tilde{Y}_m}{W_m} \tilde{T} \\ \bar{\tau}_{ij} &\approx \mu \left(\frac{\partial \tilde{u}_i}{\partial x_j} + \frac{\partial \tilde{u}_j}{\partial x_i} \right) - \frac{2}{3} \delta_{ij} \mu \frac{\partial \tilde{u}_k}{\partial x_k} \\ \frac{\partial}{\partial x_j} [\overline{\tau_{ij} u_i} - \bar{\tau}_{ij} \tilde{u}_i] &\approx \frac{\partial}{\partial x_j} \left(\mu \frac{\partial \tilde{k}}{\partial x_j} \right) \\ \bar{q}_j &\approx -\lambda_{tr} \frac{\partial \tilde{T}_{tr}}{\partial x_j} - \lambda_{ve} \frac{\partial \tilde{T}_{ve}}{\partial x_j} - \bar{\rho} D \sum_{m=1}^{ns} h_m(\tilde{T}_{tr}, \tilde{T}_{ve}) \frac{\partial \tilde{Y}_m}{\partial x_j} \\ \bar{q}_{ve,j} &\approx -\lambda_{ve} \frac{\partial \tilde{T}_{ve}}{\partial x_j} - \bar{\rho} D \sum_{m=1}^{ns} h_{ve,m}(\tilde{T}_{ve}) \frac{\partial \tilde{Y}_m}{\partial x_j} \\ \bar{\rho} \tilde{Y}_m \tilde{V}_j^{(m)} + \left[\overline{\rho Y_m'' V_j^{(m)''}} - \bar{\rho} \tilde{Y}_m \tilde{V}_j^{(m)} \right] &\approx \bar{\rho} D \frac{\partial \tilde{Y}_m}{\partial x_j} \end{aligned} \quad (67)$$

5 Hybrid RAS/LES Closures

The LES approach for turbulence closure attempts to resolve the large scale components of turbulence while modeling the smaller scales. Given that most of the transport of mass, momentum, and energy is carried out by the large eddies, this strategy has the potential to remove most of the burden suffered by RAS closures that must model the entire range of turbulence scales. Unfortunately, the computational cost of LES often prohibit its use as an engineering tool for practical applications that involve attached wall boundary layer flows. In attached flow regions, the range of turbulence scales near the surface is greatly reduced, requiring grid densities (locally) approaching that required for DNS in order to resolve a significant fraction of the turbulence. This observation has fueled the development of hybrid approaches that attempt to utilize RAS in regions where the turbulence closure models are expected to be adequate (e.g., attached boundary layer flows), and only resort to a scale-resolving strategy in regions of the flow where the accuracy of RAS is likely to break down (e.g., free shear flows and regions of massive flow separation). A comparison of the LES and RAS equations reveals that the two equation sets share the same overall structure allowing for a plethora of options for blending LES and RAS into a single modeling strategy for complex flows of engineering interest.

Spalart et al.¹³ proposed a hybrid methodology they refer to as Detached Eddy Simulation (DES), in which a RAS closure is invoked near solid surfaces where the flow is attached, and a grid resolution dependent SGS closure is invoked for separated (detached) flow regions. The original DES concept was built around the Spalart Allmaras one-equation turbulence model, where the transition to an SGS closure was accomplished by altering the length scale that appears in the turbulent transport equation of $\tilde{\nu}$ (see Appendix D). The base RAS model uses the wall distance, d , as the turbulence length scale. The DES model replaces this length scale with the minimum of d and the DES filter width defined as

$$\Delta_{DES} = C_{DES} \Psi \Delta_{max}, \quad \Delta_{max} = \text{MAX}[\Delta_x, \Delta_y, \Delta_z] \quad (68)$$

where C_{DES} is an empirical constant, and Ψ is a low Reynolds number correction defined by the expression below.

$$\Psi^2 = \text{MIN} \left[10^2, \frac{1 - \frac{c_{b1}}{c_{w1} k^2 f_w^*} [f_{t2} + f_{v2} (1 - f_{t2})]}{f_{v1} \text{MAX}[10^{-10}, 1 - f_{t2}]} \right] \quad (69)$$

The quantity f_w^* represents the equilibrium value of the function f_w in the Spalart Allmaras closure, and takes on the value of 0.424. The DES approach was later extended to a two-equation (Menter $k-\omega$) formulation by Strelets.¹⁴ The two-equation DES formulation replaces the RAS turbulence length scale that appears in the destruction term of the turbulent kinetic energy equation, i.e.,

$$C_{k_d} \bar{\rho} \tilde{k} \tilde{\omega} \equiv C_{k_d} \bar{\rho} \frac{\tilde{k}^{\frac{3}{2}}}{\tilde{l}}, \quad \tilde{l} \equiv \frac{\sqrt{\tilde{k}}}{C_{k_d} \tilde{\omega}} \quad (70)$$

with the DES length scale defined by the following expression.

$$\hat{l} = \text{MIN}[\tilde{l}, \Delta_{DES}] \quad (71)$$

In principle, this modification can be made to convert any two-equation RAS model to a DES formulation, so this option can be invoked with any of the linear k - ω models (Menter-BSL, Menter-SST, Wilcox-1998, and Wilcox-2006) that are available in VULCAN-CFD. However, the low Reynolds number modification (Ψ) is only applied in VULCAN-CFD when the Spalart Allmaras model is chosen as the base RAS model.

A major drawback to the original DES approach that was highlighted from the formulation's inception appears when the grid is locally refined in multiple directions in regions not intended to be scale-resolved. This scenario often arises where grid refinement is required in some region of high geometric curvature or near junctures where multiple solid surfaces coalesce. Given that the DES transition criteria (Eq. 71) directly compares the RAS length scale to the maximum grid cell length, the eddy viscosity may be substantially reduced in the boundary layer if the grid is locally refined in all directions with no mechanism to transfer the modeled turbulence energy into resolved energy. In this scenario, the flow effectively relaminarizes, corrupting the properties of the turbulent boundary layer. As a result, the early successes of the original DES formulation typically involved flow applications with relatively simple geometries where this set of circumstances can often be avoided. This can represent a severe limitation, however, for complex flow applications where local refinements are often unavoidable.

Based on this observation, one would prefer to base the blending strategy on local flow properties as well as grid spacing to take some of the burden away from the grid generation process. The intended use of DES was to have the model act in RAS mode for attached wall-bounded flow regions and blend into an LES formulation for detached (separated or free shear) flow regions. This scenario is quite similar to what Menter¹⁵ faced in his work toward blending the k - ω and k - ϵ models. Menter sought to develop a single RAS turbulence model that retained the robustness and accuracy of the Wilcox k - ω model for wall-bounded viscous regions, while enforcing a k - ϵ model away from solid surfaces to avoid the undesirable dependence of k - ω model results on freestream values of ω . To achieve this goal, Menter linearly combined the k - ω and k - ϵ model equations with a blending function designed to yield a value of 1 near solid surfaces, and rapidly transition to 0 in the outer portion of the boundary layer and regions of free shear. This idea was adapted to provide a hybrid RAS/LES framework,¹⁶ with a variety of advancements documented in subsequent research efforts.^{17,18} The motivation behind the development of this hybrid RAS/LES framework is twofold. First, the blending of two independent RAS and LES closure models offers the flexibility of having an optimized set of closure equations for both RAS and LES modes. The second (and more critical) driving factor was the desire to alleviate the difficulties associated with the design of grid topologies that are appropriate for purely grid dependent blending paradigms. The details of this hybrid RAS/LES framework (as implemented in VULCAN-CFD) are provided in Appendix F.

Several modifications to the basic DES concept have also been proposed by the DES research community to address the shortcomings of the original formulation (including the major one described above). The most recent incarnation of the DES formulation is termed Improved Delayed Detached Eddy Simulation (IDDES). The original Shur et al.¹⁹ IDDES formulation (see Appendix G) is available in VULCAN-CFD for use with the Spalart Allmaras one-equation RAS model or any linear two-equation RAS model. The low Reynolds number modification to the DES length scale²⁰ is applied when the Spalart Allmaras model is chosen as the base RAS model, but VULCAN-CFD does not currently permit the use of

IDDES for two-equation closures with low Reynolds number corrections.

6 Boundary Layer Bleed Models

The ability to control or modify boundary layers is an important issue for many aerospace applications. One of the primary boundary layer control techniques involves the removal of the low momentum flow adjacent to the wall via a bleed system. This has the effect of moving high momentum flow closer to the surface, resulting in a boundary layer that is more resistant to separation. The direct simulation of boundary layer bleed systems is not a trivial task. Bleed systems are characterized by porous surfaces that are composed of many (on the order of hundreds or more) discrete flow passages. These passages are typically small relative to the boundary layer thickness so that it is often intractable to resolve each of them discretely. To overcome this, models have been developed to account for the effects of bleed on the flow, without resorting to resolving all of the geometric details of the porous wall.

The common practice in effusion modeling^{21,22} is to enforce bleed/effusion via the specification of a boundary condition. This strategy forces the dependent variables at all grid cell faces attached to the bleed surface to be set to some averaged state that matches the desired effusion flow rate. VULCAN-CFD uses a different approach²³ where the boundary layer effusion is accomplished through the introduction of source (or sink) terms in the grid cells adjacent to the bleed region of interest. The source terms account for the flux of mass, momentum, and energy of the fluid flow passing through the bleed passages without requiring an averaging operator to relate these fluxes to an effective flux across the entire cell area. This approach allows the surface boundary condition (e.g., slip wall, isothermal wall, adiabatic wall) to remain unchanged in the presence of bleed and is consistent with the observation that the porosity of practical bleed systems is relatively small (typically on the order of 20% or less). In other words, from a macroscopic viewpoint, the bleed region would appear mostly as a solid surface. Another advantage of accounting for bleed via source terms is that it offers a direct path to add empirical models for turbulent (or viscous) effects.

The source terms added to the governing equations are expressed as

$$\begin{aligned}
 \text{continuity} &\rightarrow \dot{m}_h \cdot Y_h^m & (72) \\
 \text{momentum} &\rightarrow \dot{m}_h \cdot u_h^i + A_h^i (P_h - P_w) \\
 \text{energy} &\rightarrow \dot{m}_h \cdot H_h
 \end{aligned}$$

where \dot{m}_h is the mass flow rate through the bleed holes associated with a given bleed cell interface, Y_h^m is the mass fraction of species “ m ” passing through the bleed holes, and (u_h^i, P_h, H_h) are the velocity components, pressure, and total enthalpy of the bleed hole fluid. The inclusion of the wall pressure (P_w) in the source term for the momentum equations is meant to remove the flux contribution from the surface pressure acting on the portion of the surface occupied by the bleed orifices (erroneously introduced when evaluating the inviscid fluxes). Two different effusion formulations are available in VULCAN-CFD to determine the bleed hole properties ($\dot{m}_h, Y_h^m, u_h^i, P_h,$ and H_h). One formulation is due to Doerffer and Bohning,²¹ and the other is a formulation developed by Slater.²² Both bleed models are described in Appendix H.

The final aspect of the effusion model framework is the inclusion of a plenum (modeled as a control volume) to balance the flow rates entering (or exiting) the computational domain with those exiting (or entering) from some external source. The process is shown schematically in Fig. 1.

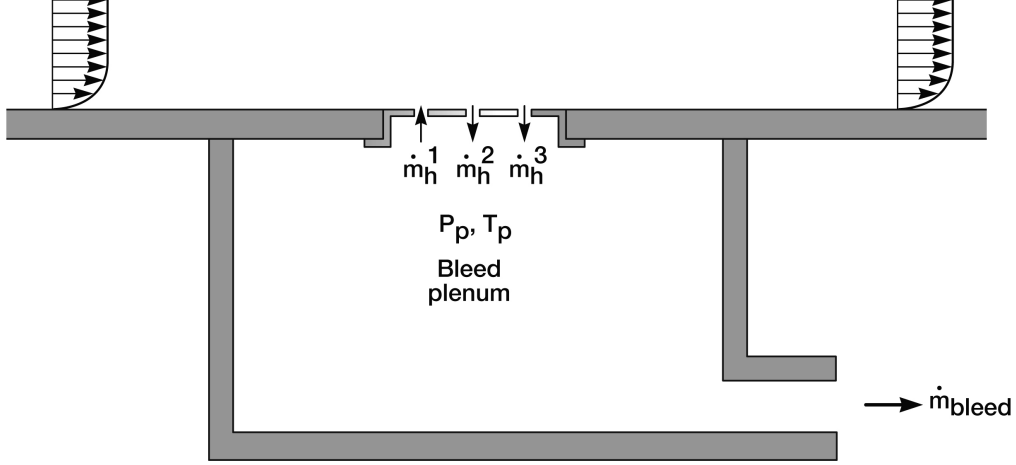


Figure 1: Schematic of effusion process including the plenum (modeled as a control volume).

The plenum properties, which are required for both effusion models described above, are determined by considering the balance of flow rates entering and exiting the plenum

$$\frac{d}{dt}(\rho_p) = \frac{1}{V_p} \left(\dot{m}_{bleed} + \sum_{n=1}^{n_{cells}} \dot{m}_h \right) \quad (73)$$

where n_{cells} is the number of grid cells in the computational domain that interface with the plenum, ρ_p is the plenum fluid density, V_p is the plenum volume, and \dot{m}_{bleed} is the specified effusion flow rate exiting (or entering) the plenum. The sign convention for the mass flow rate is positive for flow exiting the plenum and negative for flow entering the plenum. In a similar fashion, the energy (E_p) and composition (Y_p^m) of the plenum gas are determined from the following relationships.

$$\frac{d}{dt}(\rho_p E_p) = \frac{1}{V_p} \left(\dot{m}_{bleed} \cdot H + \sum_{n=1}^{n_{cells}} \dot{m}_h \cdot H_h \right) \quad (74)$$

$$\frac{d}{dt}(\rho_p Y_p^m) = \frac{1}{V_p} \left(\dot{m}_{bleed} \cdot Y_m + \sum_{n=1}^{n_{cells}} \dot{m}_h \cdot Y_h^m \right) \quad (75)$$

The values for H and Y_m are simply the current plenum values if flow is drawn out of the plenum ($\dot{m}_{bleed} > 0$). If flow is supplied to the plenum ($\dot{m}_{bleed} < 0$), the values for H and Y^m must be specified. The integration of Eqs. 73, 74, and 75 are sufficient to describe the thermodynamic state of the plenum. However, the plenum pressure is underrelaxed to improve the robustness of the solution procedure, i.e.,

$$P_p^{new} = r P_p^{new} + (1 - r) P_p^{old}, \quad (0 < r \leq 1) \quad (76)$$

where r is the chosen relaxation parameter.

7 Performance Extraction Methods

The use of CFD for the design and analysis of propulsion systems often requires the extraction of “one-dimensional” figures of merit (e.g., total pressure recovery, mixing and combustion efficiency) from simulation data. The extraction of one-dimensional properties from multidimensional simulation data is realized by applying some sort of data reduction technique to a family of computational surfaces (or lines in two dimensions) as illustrated in Fig. 2. The surfaces of interest will generally correspond to the crossflow planes of the propulsion system flowpath. A variety of data reduction techniques exist for the extraction of performance measures from multidimensional data sets. However, certain aspects of the multidimensional information are inevitably lost in the data reduction process. As a result, the unique assumptions associated with a given approach should be well understood to determine the best data reduction strategy for the intended purpose of the performance extraction.

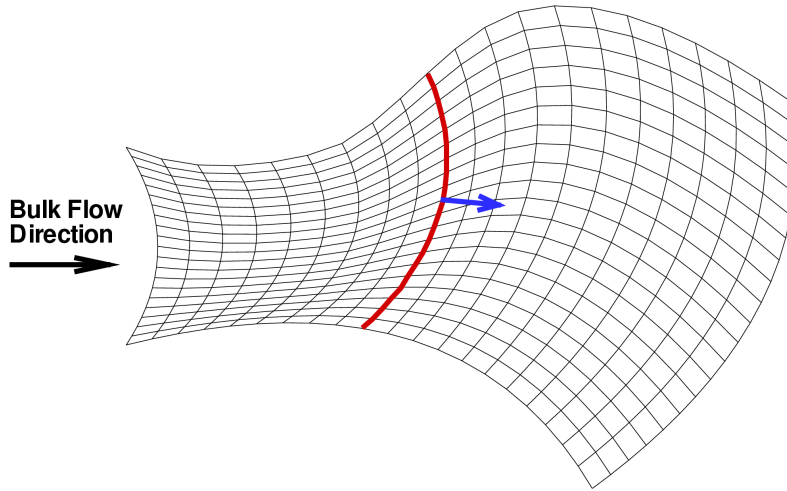


Figure 2: Surface of integration and the unit normal for the extraction of system performance metrics.

One-dimensionalization techniques can be categorized as either a weighted or flux-based approach. Weighted approaches can generally be expressed as

$$\phi = \frac{\int \phi w dA}{\int w dA} \quad (77)$$

where ϕ is the flow property to be one-dimensionalized, w is the weight factor, and A is the area over which the integration is being performed. Popular choices for the weight factor are area weighting ($w = 1$) and mass flux weighting ($w = \rho (\vec{v} \cdot \vec{n})$). The weighted approaches are easy to implement, tend to yield 1-D properties that “visually” mimic the original multidimensional data, and tend to maintain the qualitative physical features of the

parent multidimensional flow (e.g., nondecreasing entropy changes). The dilemma with these approaches is that the fluxes reconstructed from the weighted variables will, in general, not match those from the multidimensional data set. As a result, this data reduction approach is not well suited for coupling a multidimensional analysis with one-dimensional engineering analysis tools. Flux-based approaches attempt to address this deficiency by formulating a set of one-dimensional flow properties that recovers some specified set of fluxes from the multidimensional data set. Popular flux-based approaches include: the Conserved Mass/Momentum/Energy (CMME) method,²⁴ Conserved Mass/Momentum/Energy method with flow distortion,^{25,26} and the Conserved Mass/Energy/Entropy (CMES) method (also referred to as the thermodynamic state average).^{27,28}

The CMME method produces a set of uniform flow properties that satisfy the integral relations for conservation of mass, momentum, and energy, i.e.,

$$f_{mass}^m = \int [\rho (\vec{v} \cdot \vec{n}) Y_m] dA \quad (78a)$$

$$\vec{f}_{momentum} = \int [\rho (\vec{v} \cdot \vec{n}) \vec{v} + P \vec{n}] dA \quad (78b)$$

$$f_{energy} = \int [\rho (\vec{v} \cdot \vec{n}) h_o] dA \quad (78c)$$

where f represents the flux quantities being conserved, ρ is the mixture density, \vec{v} is the velocity vector, \vec{n} is the unit vector normal to the surface of integration, Y_m is the mass fraction of species “ m ”, P is the static pressure, and h_o is the total enthalpy (sum of the static enthalpy and kinetic energy). The uniform flow properties that satisfy these integral flux relations are defined based on the following expressions

$$f_{mass}^m = [\rho (\vec{v} \cdot \vec{n}) Y_m] \mathbf{A} \quad (79a)$$

$$\vec{f}_{momentum} = [\rho (\vec{v} \cdot \vec{n}) \vec{v} + \mathbf{P} \vec{n}] \mathbf{A} \quad (79b)$$

$$f_{energy} = [\rho (\vec{v} \cdot \vec{n}) h_o] \mathbf{A} \quad (79c)$$

where the bold-faced quantities denote one-dimensional properties. The equation set is closed by introducing an equation of state, e.g., $\mathbf{P} = \rho \mathbf{RT}$. This method results in a non-linear system of coupled equations, and the procedure used to decode the one-dimensional flow properties from this equation set is given in Appendix I. Note that the decomposition process for this methodology satisfies each individual component of the momentum flux vector. As a result, this approach produces decomposed flow properties that are best characterized as an effective uniform flow representation of the parent multidimensional flowfield, rather than a true one-dimensionalization of the flowfield. In other words, the decomposition process allows for the extraction of independent u , v , and w velocity components without any user specified information about the desired (streamwise) direction of the one-dimensionalized flowfield.

The CMME method with the Langley distortion methodology²⁵ satisfies the same flux expressions given in Eq. 78, but additional flux relations are introduced to provide information on the impact of multidimensional effects (i.e., flow distortion). The additional flux relations are the mass flux weighted kinetic energy components, $\int \rho (\vec{v} \cdot \vec{n}) u^2 dA$,

$\int \rho (\vec{v} \cdot \vec{n}) v^2 dA$, $\int \rho (\vec{v} \cdot \vec{n}) w^2 dA$, and the pressure force components, $\int P \vec{n} dA$. This additional information simplifies the decomposition process, since the velocity (via the kinetic energy components) and the pressure are readily available, but results in an overconstrained system of equations. Additional unknowns (distortion parameters) are introduced to allow the uniform flow properties to simultaneously satisfy these constraints and the desired conservation relationships (Eq. 78). The uniform flow properties obtained from the Langley distortion methodology satisfy the following expressions,

$$f_{mass}^m = [\rho (\vec{v} \cdot \vec{n}) \eta_1 \mathbf{Y}_m] \mathbf{A} \quad (80a)$$

$$f_{momentum} = [\rho (\vec{v} \cdot \vec{n}) \eta_2 (\vec{v} \cdot \vec{n}) + \eta_4 P_{ref}] \mathbf{A} \quad (80b)$$

$$f_{energy} = [\rho (\vec{v} \cdot \vec{n}) \eta_1 (\mathbf{h} + \eta_3 (\vec{v} \cdot \vec{n})^2 / 2)] \mathbf{A} \quad (80c)$$

where

$$\eta_1 = \frac{\int \rho (\vec{v} \cdot \vec{n}) dA}{\rho (\vec{v} \cdot \vec{n}) \mathbf{A}} \quad (81a)$$

$$\eta_2 = \frac{\int \rho (\vec{v} \cdot \vec{n}) (\vec{v} \cdot \vec{n}) dA}{\rho (\vec{v} \cdot \vec{n}) (\vec{v} \cdot \vec{n}) \mathbf{A}} \quad (81b)$$

$$\eta_3 = \frac{(\vec{v} \cdot \vec{v})}{(\vec{v} \cdot \vec{n})^2} \quad (81c)$$

$$\eta_4 = \frac{\mathbf{P}}{P_{ref}} \quad (81d)$$

define the distortion parameters that appear. In principle, P_{ref} can be tailored to force the pressure to follow a desired thermodynamic path (e.g., a path that recovers the entropy flux from the parent multidimensional flowfield). In practice, however, η_4 is typically defined as unity (i.e., $\mathbf{P} = P_{ref}$). Note that the momentum equation (a vector expression) has been reduced to a scalar equation by taking the dot product of this vector with the unit vector, \vec{n} . Hence, the resulting uniform flow properties represent a true one-dimensionalization of the multidimensional parent flowfield with the flow direction dictated by the choice of this unit vector. It can be shown that this methodology (with $\eta_4 = 1$) results in uniform properties that are analogous to those obtained based on the following operations:

- Area weighting the pressure (using the area projection perpendicular to the 1-D direction, i.e., $w = \vec{n} \cdot \vec{n}$)
- Mass flux weighting the mean kinetic energy components
- Mass flux weighting the static enthalpy
- Thermodynamic closure with an equation of state

The CMME method with the Air Force Research Laboratory (AFRL) distortion methodology²⁶ is similar to the Langley distortion method discussed above. In this approach, the pressure force components ($\int P \vec{n} dA$) must be supplied in addition to the flux expressions

given in Eq. 78. The uniform flow properties obtained from this distortion methodology satisfy the following expressions,

$$f_{mass}^m = [\rho (\vec{v} \cdot \vec{n}) \eta_1 \mathbf{Y}_m] \mathbf{A} \quad (82a)$$

$$f_{momentum} = [\rho (\vec{v} \cdot \vec{n}) \eta_1 (\vec{v} \cdot \vec{n}) + \mathbf{P}] \mathbf{A} \quad (82b)$$

$$f_{energy} = [\rho (\vec{v} \cdot \vec{n}) \eta_1 (\mathbf{h} + \eta_2 (\vec{v} \cdot \vec{n})^2 / 2)] \mathbf{A} \quad (82c)$$

where

$$\eta_1 = \frac{\int \rho (\vec{v} \cdot \vec{n}) dA}{\rho (\vec{v} \cdot \vec{n}) \mathbf{A}} \quad (83a)$$

$$\eta_2 = \frac{(\vec{v} \cdot \vec{v})}{(\vec{v} \cdot \vec{n})^2} \quad (83b)$$

define the distortion parameters that appear. Note that the momentum equation has been reduced to a scalar equation by taking the dot product of this vector with the unit vector, \vec{n} . As a result, the uniform flow properties extracted by this method represent a true one-dimensionalization of the multidimensional parent flowfield with the flow direction dictated by the choice of this unit vector. It can be shown that this methodology results in uniform properties that are analogous to those obtained based on the following operations:

- Area weighting the pressure (using the area projection perpendicular to the 1-D direction, i.e., $w = \vec{n} \cdot \vec{n}$)
- Mass flux weighting the velocity components
- Mass flux weighting the static enthalpy
- Thermodynamic closure with an equation of state

The CMES method (or thermodynamic state average) was first introduced by Riggins et al.^{27,28} The primary motivation behind this method was to address the deficiencies of the existing conserved-flux approaches as related to violations of the second law of thermodynamics. The CMME method (with or without distortion effects) introduces an entropy increase due solely to the “mixing loss” associated with the one-dimensionalization process. The CMES method attempts to rectify this problem by explicitly conserving the entropy flux obtained from the parent multidimensional flowfield,

$$f_{entropy} = \int [\rho (\vec{v} \cdot \vec{n}) s] dA \quad (84)$$

and as a result, this method provides uniform flow properties that satisfy the integral relations for conservation of mass, energy, and entropy.

$$f_{mass}^m = [\rho (\vec{v} \cdot \vec{n}) \mathbf{Y}_m] \mathbf{A} \quad (85a)$$

$$f_{energy} = [\rho (\vec{v} \cdot \vec{n}) \mathbf{h}_o] \mathbf{A} \quad (85b)$$

$$f_{entropy} = [\rho (\vec{v} \cdot \vec{n}) \mathbf{s}] \mathbf{A} \quad (85c)$$

The conservation of these fluxes ensures equivalency of mass addition, heating, and irreversible losses between the parent multidimensional flowfield and the one-dimensional flowfield. This statement holds regardless of the level (or type) of flow distortion that may be present because changes in mass, total enthalpy, and entropy are not influenced by flow distortion. Changes in these fluxes can only occur due to mass and/or heat addition (or extraction) and irreversible phenomena. The momentum flux, on the other hand, is affected by flow distortion, and its impact on the stream-thrust is accounted for in this method via the introduction of a single distortion parameter, η . This distortion parameter is defined in a manner that forces a match between the multidimensional stream-thrust and the one-dimensional value.

$$\int [\rho (\vec{v} \cdot \vec{n}) \vec{v} + P \vec{n}] \cdot \vec{n} dA = \eta [\rho (\vec{v} \cdot \vec{n}) (\vec{v} \cdot \vec{n}) + P] A \quad (86)$$

Similar to the distortion methodologies described previously, the uniform flow properties that result from this method represent a true one-dimensionalization of the multidimensional simulation data, and the amount of distortion that is present in the flow is influenced by the choice of the unit vector, \vec{n} . The procedure used to decode the one-dimensional flow properties for the CMES approach is given in Appendix I.

References

1. Gnoffo, P. A., Gupta, R. N., and Shinn, J. L.: Conservation Equations and Physical Models for Hypersonic Air Flows in Thermal and Chemical Nonequilibrium. NASA Technical Paper 2867, Feb. 1989.
2. Millikan, R. C. and White, D. R.: Systematics of Vibrational Relaxation. *Journal of Chemical Physics*, vol. 39, no. 12, 1963, pp. 3209–3213.
3. Park, C.: Review of Chemical-Kinetic Problems of Future NASA Missions, I: Earth Entries. *Journal of Thermophysics and Heat Transfer*, vol. 7, no. 3, 1993, pp. 385–398.
4. Park, C.: Problems of Rate Chemistry in the Flight Regimes of Aeroassisted Orbital Transfer Vehicles. AIAA Paper 84-1730, 1984.
5. Park, C.: Assessment of Two-Temperature Kinetic Model for Ionizing Air. AIAA Paper 87-1574, 1987.
6. Huang, P. G., Coleman, G. N., and Bradshaw, P.: Compressible Turbulent Channel Flow - A Close Look Using DNS Data. AIAA Paper 95-0584, Jan. 1995.
7. Pope, S. B.: PDF Methods for Turbulent Reactive Flows. *Progress in Energy Combustion Science*, vol. 11, 1985, pp. 119–192.
8. Peters, N.: Laminar Flamelet Concepts in Turbulent Combustion. *Proceedings of the Twenty-First Symposium (International) on Combustion*, vol. 21, 1986, pp. 1231–1250.
9. Kerstein, A. R.: Linear Eddy Model of Turbulent Scalar Transport and Mixing. *Combustion Science and Technology*, vol. 60, 1988, pp. 391–421.

10. Bilger, R. W.: Conditional Moment Closure for Turbulent Reacting Flow. *Physics of Fluids*, vol. 5, no. 2, 1993, pp. 436–444.
11. Magnussen, B. F. and Hjertager, B. H.: On Mathematical Modeling of Turbulent Combustion with Special Emphasis on Soot Formation and Combustion. *Sixteenth Symposium (International) on Combustion*, 1976, pp. 719–729.
12. Pope, S. B.: *Turbulent Flows*. Cambridge University Press, 2000.
13. Spalart, P. R., Jou, W.-H., Strelets, M. K., and Allmaras, S. R.: Comments on the Feasibility of LES for Wings, and on a Hybrid RANS/LES Approach. 1st AFOSR International Conference on DNS/LES (invited), Aug. 1997.
14. Strelets, M. K.: Detached Eddy Simulation of Massively Separated Flows. AIAA Paper 2001-0879, Jan. 2001.
15. Menter, F. R.: Zonal Two Equation k - ω Models for Aerodynamic Flows. AIAA Paper 93-2906, July 1993.
16. Baurle, R. A., Tam, C.-J., Edwards, J. R., and Hassan, H. A.: Hybrid Simulation Approach for Cavity Flows: Blending, Algorithm, and Boundary Treatment Issues. *AIAA Journal*, vol. 41, no. 8, Aug. 2003, pp. 1463–1480.
17. Choi, J.-L., Edwards, J. R., and Baurle, R. A.: Compressible Boundary Layer Predictions at High Reynolds Number Using Hybrid LES/RANS Methods. *AIAA Journal*, vol. 47, no. 9, 2009, pp. 2179–2193.
18. Boles, J. A., Edwards, J. R., Choi, J.-L., and Baurle, R. A.: Simulations of High-Speed Internal Flows Using LES/RANS Models. AIAA Paper 2009-1324, Jan. 2009.
19. Shur, M. L., Spalart, P. R., Strelets, M. K., and Travin, A. K.: Detached-Eddy Simulation of an Airfoil at High Angle of Attack. 4th Int. Symp. Eng. Turb. Modeling and Measurements, May 1999.
20. Spalart, P. R., Deck, S., Shur, M. L., Squires, K. D., Strelets, M. K., Travin, A. K.: A New Version of Detached-Eddy Simulation, Resistant to Ambiguous Grid Densities. *Theoretical Computational Fluid Dynamics*, vol. 20, no. 3, 2006, pp. 181–195.
21. Doerffer, P. P. and Bohning, R.: Modelling of Perforated Plate Aerodynamics Performance. *Aerospace Science and Technology*, vol. 4, no. 8, Nov. 2000, pp. 525–534.
22. Slater, J. W.: Improvements in Modeling 90-degree Bleed Holes for Supersonic Inlets. AIAA Paper 2009-0710, Jan. 2009.
23. Baurle, R. A. and Norris A. T.: A Source-Term Based Boundary Layer Bleed/Effusion Model for Passive Shock Control. 2011 JANNAF JPM/CS/APS/EPSS/PSHS Meeting, April 2011.
24. Riggins, D. W. and McClinton, C. R.: Analysis of Losses in Supersonic Mixing and Reacting Flows. AIAA Paper 91-2266, June 1991.

25. Auslender, A. H.: An Application of Distortion Analysis to Scramjet-Combustor Performance Assessment. *Scramjet Engine Performance Analysis, Evaluation, and Optimization – JANNAF Propulsion and Joint Subcommittee Scramjet Performance Workshop*, Dec. 1996.
26. Davis, D. L., Hagenmaier, M. A., and Risha D.: Computational Fluid Dynamics Data Reduction Methods for Scramjet Performance Analysis. WPAFB Report, Oct. 1997.
27. Riggins, D. W., McClinton, C. R., and Vitt, P. H.: Thrust Losses in Hypersonic Engines Part 1: Methodology. *Journal of Propulsion and Power*, vol. 13, no. 2, March-April 1997, pp. 281–287.
28. Riggins, D. W.: Thrust Losses in Hypersonic Engines Part 2: Applications. *Journal of Propulsion and Power*, vol. 13, no. 2, March-April 1997, pp. 288–295.
29. McBride, B. J. and Gordon, S.: Computer Program for Calculation of Complex Chemical Equilibrium Composition and Applications, I. Analysis. NASA Reference Publication 1311, Oct. 1994.
30. McBride, B. J. and Gordon, S.: Computer Program for Calculation of Complex Chemical Equilibrium Composition and Applications, II. Users Manual and Program Description. NASA Reference Publication 1311, June 1996.
31. Sutherland, W.: The Viscosity of Gases and Molecular Force. *Philosophical Magazine*, vol. 36, no. 223, 1893, pp. 507–531.
32. Dorrance, W. H.: *Viscous Hypersonic Flow*. McGraw-Hill, 1962.
33. Mason, E. A. and Saxena, S. C.: Approximate Formula for the Thermal Conductivity of Gas Mixtures. *Physics of Fluids*, vol. 1, no. 5, 1958, pp. 361–369.
34. Vincenti, W. G. and Kruger, C. H.: *Introduction to Physical Gas Dynamics*. John Wiley and Sons, 1965.
35. Lindemann, F. A., Arrhenius, S., Langmuir, I., Dhar, N. R., Perrin, J., and Lewis, W. C. McC.: The Radiation Theory of Chemical Action. *Transactions of the Faraday Society*, vol. 17, 1922, pp. 598–606.
36. Stewart, P., H., Larson, C. W., and Golden, D. M.: Pressure and Temperature Dependence of Reactions Proceeding via a Bound Complex. 2. Application to $2\text{CH}_3 \rightarrow \text{C}_2\text{H}_5 + \text{H}$. *Combustion and Flame*, vol. 75, no. 1, 1989, pp. 25–31.
37. Troe, J.: Theory of Thermal Unimolecular Reactions in the Fall-Off Range. I. Strong Collision Rate Constants. *Ber. Bunsenges. Phys. Chem.*, vol. 87, 1983, pp. 161–169.
38. Gilbert, R. G., Luther, K., and Troe, J.: Theory of Thermal Unimolecular Reactions in the Fall-Off Range. II. Weak Collision Rate Constants. *Ber. Bunsenges. Phys. Chem.*, vol. 87, 1983, pp. 169–177.
39. Wilcox, D. C.: *Turbulence Modeling for CFD*. DCW Industries, Inc., 3rd ed., 2006.

40. Spalart, P. R. and Allmaras, S. R.: A One-Equation Turbulence Model for Aerodynamic Flows. AIAA Paper 92-0439, Jan. 1992.
41. Spalart, P. R. and Allmaras, S. R.: A One-Equation Turbulence Model for Aerodynamic Flows. *Recherche Aerospaciale*, 1994, pp. 5–21.
42. Menter, F. R.: Two-Equation Eddy-Viscosity Turbulence Models for Engineering Applications. *AIAA Journal*, vol. 32, no. 8, 1994, pp. 1598–1605.
43. Wilcox, D. C.: *Turbulence Modeling for CFD*. DCW Industries, Inc., 2nd ed., 1998.
44. Spalart, P. R.: Philosophies and Falacies in Turbulence Modeling. *Progress in Aerospace Sciences*, vol. 74, 2015, pp. 1–15.
45. Rumsey, C. L. and Gatski, T. B.: Summary of EASM Turbulence Models in CFL3D with Validation Test Cases. NASA Technical Report TM-2003-212431, 2003.
46. Wilcox, D. C.: Wall Matching, a Rational Alternative to Wall Functions. AIAA Paper 89-0611, Jan. 1989.
47. Papamoschou, D. and Roshko, A.: The Compressible Turbulent Shear Layer - An Experimental Study. *Journal of Fluid Mechanics*, vol. 197, 1988, pp. 453–477.
48. Smagorinsky, J.: General Circulation Experiments with the Primitive Equations. *Monthly Weather Review*, vol. 91, no. 3, March 1963, pp. 99–164.
49. Vreman, A. W.: An Eddy-Viscosity Subgrid-Scale Model for Turbulent Shear Flow: Algebraic Theory and Applications. *Physics of Fluids*, vol. 16, no. 10, Oct. 2004, pp. 3670–3681.
50. Yoshizawa, A. and Horiuti, K.: A Statistically-Derived Subgrid Scale Kinetic Energy Model for Large-Eddy Simulation of Turbulent Flows. *Journal of the Physical Society of Japan*, vol. 54, 1985, pp. 2834–2839.
51. Germano, M., Piomelli, U., Moin, P., and Cabot, W. H.: A Dynamic Subgrid-Scale Eddy Viscosity Model. *Physics of Fluids*, vol. 3, no. 7, July 1991, pp. 1760–1765.
52. Heinz, S. and Gopalan, H.: Realizable Versus Non-Realizable Dynamic Subgrid-Scale Stress Models. *Physics of Fluids*, vol. 24, no. 11, Nov. 2012, pp. 1760–1765.
53. Nikitin, N. V., Nicoud, F., Wasistho, B., Squires, K. D., and Spalart, P. R.: An Approach to Wall Modeling in Large-Eddy Simulations. *Physics of Fluids*, vol. 12, July 2000, pp. 1629–1632.
54. Willis, B. P., Davis, D. O., and Hingst, W. R.: Flow Coefficient Behavior for Boundary Layer Bleed Holes and Slots. AIAA Paper 95-0031, Jan. 1995.

Appendix A

Thermodynamic Properties

The species thermodynamic properties are evaluated based on polynomial curve fits as a function of temperature.^{29,30} The specific heat at constant pressure is evaluated from the following polynomial

$$C_{p_m} = \frac{R_u}{W_m} (a_1 T^{-2} + a_2 T^{-1} + a_3 + a_4 T + a_5 T^2 + a_6 T^3 + a_7 T^4) \quad (\text{A1})$$

where a_n is a set of constants used to fit the thermodynamic property over some specified temperature range. The enthalpy of species “ m ” is defined by

$$h_m = \int_{T^\circ}^T C_{p_m} dT + \Delta h_{f_m} \quad (\text{A2})$$

where T° is the reference temperature chosen for the thermodynamic data (298.15 K) and Δh_{f_m} is the enthalpy of formation for species “ m ”. Given this definition, a polynomial fit for the species enthalpy can be obtained via integration of Eq. A1 to yield

$$h_m = \frac{R_u T}{W_m} \left(-a_1 T^{-2} + a_2 T^{-1} \ln T + a_3 + a_4 \frac{T}{2} + a_5 \frac{T^2}{3} + a_6 \frac{T^3}{4} + a_7 \frac{T^4}{5} + b_1 \right) \quad (\text{A3})$$

where the integration constant b_1 is defined such that the enthalpy of formation is recovered when h_m is evaluated at the reference temperature.

$$h_m(T^\circ) = \Delta h_{f_m} \quad (\text{A4})$$

The sensible entropy (defined at a reference pressure, P° , of one bar) is given by the following thermodynamic relationship

$$s_m = \int_{T^\circ}^T \frac{C_{p_m}}{T} dT + \Delta s_{f_m} \quad (\text{A5})$$

where Δs_{f_m} is the entropy of formation for species “ m ”. The substitution of Eq. A1 into this expression results in the following polynomial fit for the sensible entropy of species “ m ”

$$s_m = \frac{R_u}{W_m} \left(-a_1 \frac{T^{-2}}{2} - a_2 T^{-1} + a_3 \ln T + a_4 T + a_5 \frac{T^2}{2} + a_6 \frac{T^3}{3} + a_7 \frac{T^4}{4} + b_2 \right) \quad (\text{A6})$$

where the integration constant b_2 is defined such that the entropy of formation is recovered when s_m is evaluated at the reference temperature.

$$s_m(T^\circ) = \Delta s_{f_m} \quad (\text{A7})$$

The evaluation of the chemical reaction equilibrium constants requires the sensible Gibbs free energy of each species and is obtained from the following thermodynamic relationship

$$g_m = h_m - T s_m \quad (\text{A8})$$

where g_m is the Gibbs free energy of species “ m ”.

The two-temperature thermal nonequilibrium formulation, together with the assumption that the translational and rotational energy modes are fully excited (implying that their specific heats are independent of temperature), allows the polynomial fits described above to be utilized for the simulation of flows in thermal nonequilibrium. This greatly simplifies the thermodynamic relationships as compared with nonequilibrium formulations that permit additional degrees of freedom. For instance, the vibrational/electronic heat capacities for species “ m ” can be obtained by simply evaluating the polynomial fit for the species specific heat with the vibrational/electronic temperature, and subtracting out the constant translational and rotational mode contributions.

$$C_{p_{ve,m}} = C_{p_m}(T_{ve}) - C_{p_{tr,m}} \quad (\text{A9})$$

Similarly, the vibrational/electronic enthalpy and sensible entropy for each species can be obtained by evaluating the polynomial fit for enthalpy using the vibrational/electronic temperature and subtracting out the translational and rotational mode portions.

$$h_{ve,m} = h_m(T_{ve}) - C_{p_{tr,m}}(T_{ve} - T^\circ) - \Delta h_{f_m} \quad (\text{A10})$$

$$s_{ve,m} = s_m(T_{ve}) - C_{p_{tr,m}} \ln\left(\frac{T_{ve}}{T^\circ}\right) - \Delta s_{f_m} \quad (\text{A11})$$

Finally, the nonequilibrium expression for the enthalpy and entropy of each species is obtained by simply summing the contributions from the translational/rotational and vibrational/electronic modes.

$$h_m = h_{tr,m} + h_{ve,m} = C_{p_{tr,m}}(T_{tr} - T^\circ) + \Delta h_{f_m} + h_{ve,m} \quad (\text{A12})$$

$$s_m = s_{tr,m} + s_{ve,m} = C_{p_{tr,m}} \ln\left(\frac{T_{tr}}{T^\circ}\right) + \Delta s_{f_m} + s_{ve,m} \quad (\text{A13})$$

Appendix B

Transport Properties

The transport properties (μ , λ , and D) depend primarily on temperature and composition. The procedure for evaluating these quantities is to first compute the individual species values (as a function of temperature), and then combine the species coefficients to obtain a mixture-averaged value using an empirical relationship.

In VULCAN-CFD, the species molecular viscosity is evaluated using either the viscosity law of Sutherland³¹ or the polynomial fit of McBride.^{29,30} The functional form of the Sutherland law can be written as

$$\frac{\mu_m}{\mu^\circ} = \left(\frac{T}{T_\mu^\circ} \right)^{\frac{3}{2}} \frac{T_\mu^\circ + S_\mu}{T + S_\mu} \quad (\text{B1})$$

where μ° , T_μ° , and S_μ are the reference viscosity, reference temperature, and Sutherland coefficient of species “ m ”, respectively. The McBride polynomial utilizes the following functional form

$$\ln(\mu_m) = a_1 \ln T + a_2 T^{-1} + a_3 T^{-2} + a_4 \quad (\text{B2})$$

where where a_n is a set of constants used to fit the transport property over some specified temperature range. The individual species viscosity coefficients are then combined using the Wilke³² formula to yield the mixture-averaged molecular viscosity shown below.

$$\mu = \sum_{m=1}^{ns} \mu_m X_m \left[\sum_{n=1}^{ns} G_{mn} X_n \right]^{-1} \quad (\text{B3})$$

Here, X_m is the mole fraction of species “ m ”, and G_{mn} is given by the following expression.

$$G_{mn} = \frac{\left[1 + \left(\frac{\mu_m}{\mu_n} \right)^{\frac{1}{2}} \left(\frac{W_n}{W_m} \right)^{\frac{1}{4}} \right]^2}{(2)^{\frac{3}{2}} \left[1 + \left(\frac{W_m}{W_n} \right) \right]^{\frac{1}{2}}} \quad (\text{B4})$$

The thermal conductivity of each species is also evaluated using either the Sutherland or McBride functional forms. The Sutherland law for thermal conductivity is expressed as

$$\frac{\lambda_m}{\lambda^\circ} = \left(\frac{T}{T_\lambda^\circ} \right)^{\frac{3}{2}} \frac{T_\lambda^\circ + S_\lambda}{T + S_\lambda} \quad (\text{B5})$$

where λ° , T_λ° , and S_λ are the reference thermal conductivity, reference temperature, and Sutherland coefficient of species “ m ”. The McBride polynomial for thermal conductivity is analogous in form to that used for the molecular viscosity.

$$\ln(\lambda_m) = a_1 \ln T + a_2 T^{-1} + a_3 T^{-2} + a_4 \quad (\text{B6})$$

The mixture-averaged thermal conductivity is obtained through the use of the Mason and Saxena³³ formula, which can be written as

$$\lambda = \sum_{m=1}^{ns} \lambda_m X_m \left[1.065 \sum_{n=1}^{ns} (G_{mn} X_n) - 0.065 X_m \right]^{-1} \quad (\text{B7})$$

where G_{mn} is the same quantity defined in Eq. B4. Alternatively, VULCAN-CFD allows for the direct evaluation of the mixture-averaged thermal conductivity via the specification of the Prandtl number.

$$\lambda = \frac{\mu}{Pr} \quad (\text{B8})$$

The value of the diffusion coefficient is obtained by specifying the Schmidt number,

$$D = \frac{\mu}{Sc} \quad (\text{B9})$$

which assumes that the molecular diffusion coefficient is constant for all species, and is consistent with the assumptions associated with the use of Fick's law of diffusion.

The molecular viscosity only depends on the translational/rotational temperature, so for thermodynamic nonequilibrium flows, this quantity is evaluated in the same manner as that for flows in thermal equilibrium. However, the thermal conductivity contains independent translational/rotational and vibrational/electronic contributions.

$$\lambda_m = \lambda_{tr,m} + \lambda_{ve,m} \quad (\text{B10})$$

The vibrational/electronic thermal conductivity of each species is derived via the method suggested by Eucken,³⁴ which assumes that the molecular transport of the internal energy modes (rotational, vibrational, and electronic) are not correlated with the velocity. As a result, the molecular transport of the internal energy modes is similar to that of momentum transport, allowing the vibrational/electronic thermal conductivity for species “ m ” to be expressed in the following form.

$$\lambda_{ve,m} = \mu_m C_{p_{ve,m}} \quad (\text{B11})$$

The translational/rotational thermal conductivity for species “ m ” can then be obtained from

$$\lambda_{tr,m} = \lambda_m(T_{tr}) - \mu_m C_{p_{ve,m}}(T_{tr}) \quad (\text{B12})$$

where the functional form for λ_m is the desired species conductivity model (e.g., the Sutherland or McBride polynomial). The mixture-averaged conductivities for each of the energy modes are then independently evaluated based on the mixture formula of Mason and Saxena as described above.

Appendix C

Finite Rate Chemistry Extensions

The computational cost associated with tracking a large number of reacting constituents in a CFD simulation typically forces a reliance on reduced chemistry mechanisms. To minimize the number of species that must be tracked, some reduced mechanisms relax the requirement that the law of mass action utilize the stoichiometric coefficients when forming the products of species concentration. In this scenario, the rate of reaction is formulated to be proportional to the concentration of the species raised to some arbitrary power, which provides an additional degree of freedom in the chemistry reduction process. Kinetic steps constructed in this fashion are termed “arbitrary reaction order” reactions, and VULCAN-CFD allows for chemical mechanisms that employ this feature. The molar production rate of an arbitrary reaction order kinetic step (l) is expressed as

$$\left(v''_{ml} - v'_{ml} \right) \left[k_{fi} \prod_{n=1}^{ns+1} \left(\frac{\rho_n}{W_n} \right)^{v_{nl}^{*'}} - k_{bl} \prod_{n=1}^{ns+1} \left(\frac{\rho_n}{W_n} \right)^{v_{nl}^{*''}} \right] \quad (C1)$$

where $v_{nl}^{*'}$ and $v_{nl}^{*''}$ are the reaction orders provided by the reduced chemistry model.

VULCAN-CFD also includes allowances for pressure-dependent reactions. These reactions typically fall into two classes: unimolecular/recombination fall-off reactions and chemically activated bimolecular reactions. In general, the reaction rate of unimolecular/recombination fall-off reactions increases with increasing pressure. In the low pressure limit, a third body collision is needed to provide sufficient energy for the reaction to proceed, while at high pressure the third body constituent is not required. The reaction rate of chemically activated bimolecular reactions, on the other hand, decreases with increasing pressure. This kinetic process involves a competition in reaction pathways between the chemically activated bimolecular reaction and a three-body recombination reaction. In the low pressure limit, the chemically activated bimolecular reaction dominates, while the three-body recombination reaction prevails at the high pressure limit. For both classes of pressure-dependent reactions, the pure temperature-dependent Arrhenius reaction rate expressions are applicable at the pressure limits, but in between these limits the rate expressions become more complicated.

The pressure dependent reactions require standard Arrhenius reaction rate parameters for both the low (L) and high (H) pressure limits.

$$k_f^L = A^L T^{b^L} \exp\left(\frac{-T_a^L}{T}\right), \quad k_f^H = A^H T^{b^H} \exp\left(\frac{-T_a^H}{T}\right) \quad (C2)$$

The blending of these rates is then accomplished as follows

$$k_f = \begin{cases} k_f^H \left(\frac{P_r}{P_r+1} \right) F, & \text{unimolecular/recombination fall-off reactions} \\ k_f^L \left(\frac{1}{P_r+1} \right) F, & \text{chemically activated bimolecular reactions} \end{cases} \quad (C3)$$

where the reduced pressure, P_r , is defined as

$$P_r = \frac{k_f^L [M]}{k_f^H} \quad (C4)$$

and $[M]$ is the molar concentration of the third body constituent. F is an empirical factor to further control the blending between the low and high pressure limits. VULCAN-CFD supports three functional forms for F . The simplest is the Lindemann form,³⁵ where F is simply chosen to be unity. The second is the SRI form,³⁶ which defines F via the following relationship

$$F = a_4 T^{a_5} \left[a_1 \exp\left(\frac{-a_2}{T}\right) + \exp\left(\frac{-T}{a_3}\right) \right]^{\frac{1}{1+\log^2(P_r)}} \quad (\text{C5})$$

where a_1 , a_2 , a_3 , a_4 , and a_5 are input parameters that control the SRI blending mechanism. The third is the Troe form,^{37,38} which defines F as

$$\log(F) = \left[1.0 + \left(\frac{\log(P_r) - 0.4 - 0.67 \log(F_c)}{0.806 - 1.1762 \log(F_c) - 0.14 \log(P_r)} \right)^2 \right]^{-1} \log(F_c) \quad (\text{C6})$$

where

$$F_c = (1 - a_1) \exp\left(\frac{-T}{a_2}\right) + (a_1) \exp\left(\frac{-T}{a_3}\right) + \exp\left(\frac{-a_4}{T}\right) \quad (\text{C7})$$

and a_1 , a_2 , a_3 , and a_4 are the input parameters used to control the Troe blending formulation.

Appendix D

Reynolds-Averaged Turbulence Closure Models

Closure models for the Reynolds-averaged equations vary in complexity from simple algebraic (zero-equation) models, which require specification of a turbulent velocity and length scale, to full second-order closures that involve transport equations for the Reynolds stress tensor and flux vectors. Algebraic models have the advantage of being numerically robust and easy to implement (at least for relatively simple geometries), however, they often require changes in their coefficients when applied to different classes of flows, and the generalization of these models to complex geometries is not straightforward. Second-order closures (in principle) can capture a more comprehensive subset of the turbulence physics (e.g., effects of streamline curvature, rotation, swirl, stress anisotropy). Unfortunately, with few exceptions, this modeling strategy has not been shown to consistently outperform the more cost-effective eddy viscosity formulations. Moreover, the expense of a full second-order closure for chemically reacting flows can quickly become unmanageable as the number of reacting constituents increases. Based on these observations, the turbulence closure models offered in VULCAN-CFD are limited to two-equation models and “complete” (as defined by Wilcox³⁹) one-equation models.

D.1 Spalart Allmaras One-Equation Model

The Spalart Allmaras one-equation model^{40,41} solves a transport equation for the quantity $\tilde{\nu}$

$$\begin{aligned} \frac{\partial \tilde{\nu}}{\partial t} + \tilde{u}_j \frac{\partial \tilde{\nu}}{\partial x_j} = & \frac{1}{\sigma} \left[\frac{\partial}{\partial x_j} \left(\left(\frac{\mu}{\bar{\rho}} + \tilde{\nu} \right) \frac{\partial \tilde{\nu}}{\partial x_j} \right) + c_{b2} \frac{\partial \tilde{\nu}}{\partial x_j} \frac{\partial \tilde{\nu}}{\partial x_j} \right] \\ & + c_{b1} (1 - f_{t2}) \hat{S} \tilde{\nu} - \left(c_{w1} f_w - \frac{c_{b1}}{\kappa^2} f_{t2} \right) \left(\frac{\tilde{\nu}}{d} \right)^2 \end{aligned} \quad (D1)$$

and the eddy viscosity is related to this quantity as follows

$$\mu_t = \bar{\rho} \tilde{\nu} f_{v1} \quad (D2)$$

where f_{v1} is defined by the expression below.

$$f_{v1} = \frac{\left(\frac{\bar{\rho} \tilde{\nu}}{\mu} \right)^3}{\left(\frac{\bar{\rho} \tilde{\nu}}{\mu} \right)^3 + c_{v1}^3} \quad (D3)$$

The VULCAN-CFD implementation recasts the $\tilde{\nu}$ equation in strong conservation law form with the density placed inside of the outer-most derivative of the diffusion term.

$$\begin{aligned} \frac{\partial}{\partial t} (\bar{\rho} \tilde{\nu}) + \frac{\partial}{\partial x_j} (\bar{\rho} \tilde{u}_j \tilde{\nu}) = & \frac{\partial}{\partial x_j} \left[\left(\frac{\mu}{\sigma} + \frac{\bar{\rho} \tilde{\nu}}{\sigma} \right) \frac{\partial \tilde{\nu}}{\partial x_j} \right] + \bar{\rho} \frac{c_{b2}}{\sigma} \frac{\partial \tilde{\nu}}{\partial x_j} \frac{\partial \tilde{\nu}}{\partial x_j} \\ & + \bar{\rho} c_{b1} (1 - f_{t2}) \hat{S} \tilde{\nu} - \bar{\rho} \left(c_{w1} f_w - \frac{c_{b1}}{\kappa^2} f_{t2} \right) \left(\frac{\tilde{\nu}}{d} \right)^2 \end{aligned} \quad (D4)$$

This treatment of the diffusion term recovers the original nonconservation law form for incompressible flows, while providing a formulation that mimics how most developers extend their incompressible models to compressible flows. The remaining quantities are defined as

$$\begin{aligned}
\hat{S} &= \left(2\tilde{\Omega}_{ij}\tilde{\Omega}_{ij}\right)^{\frac{1}{2}} + \frac{\tilde{\nu}}{(\kappa d)^2} f_{v_2} & f_{v_2} &= 1 - \frac{\left(\frac{\tilde{\rho}\tilde{\nu}}{\mu}\right)}{1 + \left(\frac{\tilde{\rho}\tilde{\nu}}{\mu}\right)f_{v_1}} \\
f_{t_2} &= c_{t_3} \exp\left(-c_{t_4}\left(\frac{\tilde{\rho}\tilde{\nu}}{\mu}\right)^2\right) & f_w &= g \left(\frac{1+c_{w_3}}{g^6+c_{w_3}}\right)^{\frac{1}{6}} \\
g &= r + c_{w_2}(r^6 - r) & r &= \text{MIN}\left[\frac{\tilde{\nu}}{\hat{S}(\kappa d)^2}, 10\right]
\end{aligned} \tag{D5}$$

where d is the wall distance, $\tilde{\Omega}_{ij}$ is the mean rotation rate tensor, i.e.,

$$\tilde{\Omega}_{ij} = \frac{1}{2} \left(\frac{\partial \tilde{u}_i}{\partial x_j} - \frac{\partial \tilde{u}_j}{\partial x_i} \right) \tag{D6}$$

and the closure constants are provided below.

$$\begin{aligned}
\sigma &= \frac{2}{3} & \kappa &= 0.41 & c_{b_1} &= 0.1355 \\
c_{b_2} &= 0.622 & c_{w_2} &= 0.3 & c_{w_3} &= 2.0 \\
c_{v_1} &= 7.1 & c_{t_3} &= 1.2 & c_{t_4} &= 0.5 \\
c_{w_1} &= \frac{c_{b_1}}{\kappa^2} + \frac{1+c_{b_2}}{\sigma}
\end{aligned} \tag{D7}$$

Note that this model does not include a transport equation for the turbulent kinetic energy, and as a result, all closure terms involving \tilde{k} are neglected.

D.2 Menter k - ω Models

The Menter family of two-equation models⁴² blends the standard Launder-Sharma k - ϵ (transformed to a k - ω formulation) with the 1988 version of the Wilcox k - ω model. The basic idea was to retain the favorable characteristics of the Wilcox model for attached boundary layer flows, while mitigating the influence of specified freestream values of ω that has historically plagued this model. The blended Menter model equations are obtained by multiplying the transformed k - ϵ equation set by $(1 - F_1)$, the k - ω equation set by F_1 , and adding the result. The resulting equations for the turbulent kinetic energy and the specific dissipation rate can be written as

$$\begin{aligned}
\frac{\partial}{\partial t}(\bar{\rho}\tilde{k}) + \frac{\partial}{\partial x_j}(\bar{\rho}\tilde{k}\tilde{u}_j) &= \frac{\partial}{\partial x_j} \left[\left(\mu + \frac{\mu_t}{\sigma_k} \right) \frac{\partial \tilde{k}}{\partial x_j} \right] - \bar{\rho} \widetilde{u_i'' u_j''} \frac{\partial \tilde{u}_i}{\partial x_j} - C_{k_d} \bar{\rho} \tilde{k} \tilde{\omega} \\
\frac{\partial}{\partial t}(\bar{\rho}\tilde{\omega}) + \frac{\partial}{\partial x_j}(\bar{\rho}\tilde{\omega}\tilde{u}_j) &= \frac{\partial}{\partial x_j} \left[\left(\mu + \frac{\mu_t}{\sigma_\omega} \right) \frac{\partial \tilde{\omega}}{\partial x_j} \right] - C_{\omega_p} \left(\frac{C_\mu \bar{\rho}}{\mu_t} \right) \bar{\rho} \widetilde{u_i'' u_j''} \frac{\partial \tilde{u}_i}{\partial x_j} - C_{\omega_d} \bar{\rho} \tilde{\omega}^2 \\
&+ (1 - F_1) \frac{2}{\sigma_\omega^\epsilon} \left(\frac{C_\mu \bar{\rho}}{\tilde{\omega}} \right) \frac{\partial \tilde{k}}{\partial x_j} \frac{\partial \tilde{\omega}}{\partial x_j}
\end{aligned} \tag{D8}$$

where the eddy viscosity for the baseline Menter model (Menter-BSL) is provided by the expression below.

$$\mu_t = C_\mu \bar{\rho} \frac{\tilde{k}}{\tilde{\omega}} \quad (\text{D9})$$

If C^ω represents any constant in the Wilcox k - ω model (i.e., $1/\sigma_k^\omega$, C_μ^ω , ...), and C^ϵ represents any constant in the transformed k - ϵ model (i.e., $1/\sigma_k^\epsilon$, C_μ^ϵ , ...), then the corresponding constant, C , in the blended two-equation model (i.e., $\frac{1}{\sigma_k}$, C_{k_d} , ...) is expressed by the following relationship.

$$C = F_1 C^\omega + (1 - F_1) C^\epsilon \quad (\text{D10})$$

The constants of the k - ω and k - ϵ models are given in Table D1. These values reflect the VULCAN-CFD convention that defines ω as (ϵ/k) rather than the $(0.09 \epsilon/k)$ definition used by Menter.⁴²

Table D1: Menter k - ω turbulence model constants.

Constant	Wilcox k - ω	Transformed Launder-Sharma k - ϵ
κ	0.41	0.41
$1/\sigma_k$	0.5 (BSL) , 0.85 (SST)	1.0
$1/\sigma_\omega$	0.5	0.856
C_μ	0.09	0.09
C_{k_d}	1.0	1.0
C_{ω_d}	$0.075 / C_\mu^\omega$	$0.0828 / C_\mu^\epsilon$
C_{ω_p}	$C_{\omega_d}^\omega / C_{k_d}^\omega - \frac{(\kappa^\omega)^2}{\sigma_\omega^\omega} (C_\mu^\omega C_{k_d}^\omega)^{-\frac{1}{2}}$	$C_{\omega_d}^\epsilon / C_{k_d}^\epsilon - \frac{(\kappa^\epsilon)^2}{\sigma_\omega^\epsilon} (C_\mu^\epsilon C_{k_d}^\epsilon)^{-\frac{1}{2}}$

The remaining aspect of the model is the determination of the blending function, F_1 . Starting at a solid surface, F_1 should be unity over most of the boundary layer in order to preserve the desired features of the k - ω model and transition to zero near the boundary layer edge to preserve the reduced freestream dependence feature of the k - ϵ model. The following function provides the desired behavior

$$F_1 = \tanh\left(\text{arg}_1^4\right) \quad (\text{D11})$$

where the argument in the hyperbolic tangent function is provided by the following expression.

$$\text{arg}_1 = \text{MIN} \left[\text{MAX} \left[\frac{\sqrt{\tilde{k}}}{C_{k_d} \tilde{\omega} d}, \frac{500 C_\mu \mu}{\bar{\rho} \tilde{\omega} d^2} \right], \frac{4 \bar{\rho} \tilde{k}}{\sigma_\omega^\epsilon CD d^2} \right] \quad (\text{D12})$$

In the above expression, CD is the cross diffusion term in the equation governing the blended ω equation.

$$CD = \text{MAX} \left[\frac{2}{\sigma_\omega^\epsilon} \left(\frac{\bar{\rho}}{\tilde{\omega}} \right) \frac{\partial \tilde{k}}{\partial x_j} \frac{\partial \tilde{\omega}}{\partial x_j}, 10^{-20} \right] \quad (\text{D13})$$

The first argument in Equation D12 is the turbulent length scale divided by the distance to the nearest wall (d). This argument varies from 2.5 in the log region of the boundary layer, to zero at the boundary layer edge. The second argument is added to ensure F_1 does not go

to zero in the viscous sublayer. The third argument is an additional safeguard that ensures F_1 goes to zero for low values of $\tilde{\omega}$ in the freestream.

The shear stress limited version of the Menter model (Menter-SST) is identical to the baseline version described above with the exception of the expression for the eddy viscosity, which is defined below.

$$\mu_t = \frac{\bar{\rho} a_1 \tilde{k}}{\text{MAX} \left[(a_1 / C_\mu) \tilde{\omega}, F_2 \sqrt{2\tilde{\Omega}_{ij}\tilde{\Omega}_{ij}} \right]} \quad (\text{D14})$$

This expression limits the shear stress to be no greater than that given by the Bradshaw relation, which assumes the shear stress in the boundary layer to be proportional to the turbulent kinetic energy. Menter set the proportionality constant, a_1 , to 0.31 which was found to provide a good fit for adverse pressure gradient flows up to transonic and low supersonic Mach conditions. The blending function, F_2 , is present to ensure that the stress limiter is not activated in free shear flow regions. This function is similar to F_1 , but is designed to transition somewhat closer to the boundary layer edge,

$$F_2 = \tanh(\text{arg}_2^2) \quad (\text{D15})$$

and the argument in the hyperbolic tangent function is provided by the following expression.

$$\text{arg}_2 = \text{MAX} \left[\frac{2 \sqrt{\tilde{k}}}{C_{kd} \tilde{\omega} d}, \frac{500 C_\mu \mu}{\bar{\rho} \tilde{\omega} d^2} \right] \quad (\text{D16})$$

D.3 Wilcox 1998 k - ω Model

The Wilcox 1998 k - ω model⁴³ represents one of the first attempts at developing a single closure that provides good accuracy for both wall-bounded flows and all canonical free shear flows (far wakes, mixing layers, planar jets, round jets, and radial jets). Moreover, the closure is truly a “local” model (as defined by Spalart⁴⁴), since it does not rely on the wall distance parameter. The model requires the integration of transport equations for the turbulent kinetic energy and the specific dissipation rate

$$\begin{aligned} \frac{\partial}{\partial t} (\bar{\rho} \tilde{k}) + \frac{\partial}{\partial x_j} (\bar{\rho} \tilde{k} \tilde{u}_j) &= \frac{\partial}{\partial x_j} \left[\left(\mu + \frac{\mu_t}{\sigma_k} \right) \frac{\partial \tilde{k}}{\partial x_j} \right] - \bar{\rho} \widetilde{u_i'' u_j''} \frac{\partial \tilde{u}_i}{\partial x_j} - C_{kd} \bar{\rho} \tilde{k} \tilde{\omega} \quad (\text{D17}) \\ \frac{\partial}{\partial t} (\bar{\rho} \tilde{\omega}) + \frac{\partial}{\partial x_j} (\bar{\rho} \tilde{\omega} \tilde{u}_j) &= \frac{\partial}{\partial x_j} \left[\left(\mu + \frac{\mu_t}{\sigma_\omega} \right) \frac{\partial \tilde{\omega}}{\partial x_j} \right] - C_{\omega_p} \left(\frac{\tilde{\omega}}{\tilde{k}} \right) \bar{\rho} \widetilde{u_i'' u_j''} \frac{\partial \tilde{u}_i}{\partial x_j} - C_{\omega_d} \bar{\rho} \tilde{\omega}^2 \end{aligned}$$

where the eddy viscosity for this model is provided by the expression below.

$$\mu_t = C_\mu \bar{\rho} \frac{\tilde{k}}{\tilde{\omega}} \quad (\text{D18})$$

The closure coefficients associated with this model are defined as

$$\begin{aligned}
\frac{1}{\sigma_k} &= 0.5 & \frac{1}{\sigma_\omega} &= 0.5 \\
C_\mu &= 0.09 & C_{k_d} &= f_k \\
C_{\omega_d} &= \frac{9}{125} \frac{f_\omega}{C_\mu} & C_{\omega_p} &= \frac{13}{25} \\
f_k &= \begin{cases} 1 & \chi_k \leq 0 \\ \frac{1 + 680 \chi_k^2}{1 + 400 \chi_k^2} & \chi_k > 0 \end{cases} & \chi_k &= \frac{C_\mu^2}{\bar{\omega}^3} \frac{\partial \bar{k}}{\partial x_j} \frac{\partial \bar{\omega}}{\partial x_j} \\
f_\omega &= \frac{1 + 70 \chi_\omega}{1 + 80 \chi_\omega} & \chi_\omega &= \left(\frac{C_\mu}{0.09} \right)^3 \frac{|\bar{\Omega}_{ij} \bar{\Omega}_{jk} \bar{S}_{ki}|}{\bar{\omega}^3}
\end{aligned} \tag{D19}$$

where it should be noted that the values above reflect the VULCAN-CFD convention that defines ω as (ϵ/k) rather than the $(0.09 \epsilon/k)$ definition used by Wilcox.⁴³

Wilcox has also developed a version of this model that accounts for low Reynolds number effects to achieve asymptotic consistency with the expected near-wall behavior of the turbulent kinetic energy and turbulent dissipation. These modifications also allow for improved predictions of laminar to turbulent boundary layer transition (at least for incompressible flat plate flows). This variant is identical to the standard model described above, but with the C_μ , C_{k_d} , and C_{ω_p} coefficients (as they appear in Eqs. D17 and D18) modified as follows

$$\begin{aligned}
C_\mu^* &= C_\mu \left[\frac{\frac{3}{125} + \frac{Re_t}{6}}{1 + \frac{Re_t}{6}} \right] \\
C_{k_d}^* &= C_{k_d} \left[\frac{\frac{4}{15} + \left(\frac{Re_t}{8} \right)^4}{1 + \left(\frac{Re_t}{8} \right)^4} \right] \\
C_{\omega_p}^* &= C_{\omega_p} \left[\frac{\frac{1}{9} + \frac{Re_t}{2.95}}{1 + \frac{Re_t}{2.95}} \right] \left(\frac{C_\mu}{C_\mu^*} \right)
\end{aligned} \tag{D20}$$

where Re_t is the turbulence Reynolds number defined by the expression below.

$$Re_t = \frac{C_\mu \bar{\rho} \frac{\bar{k}}{\bar{\omega}}}{\mu} \tag{D21}$$

D.4 Wilcox 2006 k - ω Model

The Wilcox 2006 model³⁹ is the latest manifestation of the Wilcox k - ω formulation. The primary differences between this model and the 1998 variant are the addition of a stress limiter and an explicit cross diffusion term in the transport equation for ω . The former feature was added to improve the model predictions for adverse pressure gradient flows, while the latter feature further reduces the sensitivity of the model to freestream values

specified for ω . The transport equations for k and ω are expressed as

$$\begin{aligned}\frac{\partial}{\partial t}(\bar{\rho}\tilde{k}) + \frac{\partial}{\partial x_j}(\bar{\rho}\tilde{k}\tilde{u}_j) &= \frac{\partial}{\partial x_j} \left[\left(\mu + \frac{C_\mu \bar{\rho}\tilde{k}}{\sigma_k \tilde{\omega}} \right) \frac{\partial \tilde{k}}{\partial x_j} \right] - \bar{\rho} \widetilde{u_i'' u_j''} \frac{\partial \tilde{u}_i}{\partial x_j} - C_{k_d} \bar{\rho}\tilde{k}\tilde{\omega} \\ \frac{\partial}{\partial t}(\bar{\rho}\tilde{\omega}) + \frac{\partial}{\partial x_j}(\bar{\rho}\tilde{\omega}\tilde{u}_j) &= \frac{\partial}{\partial x_j} \left[\left(\mu + \frac{C_\mu \bar{\rho}\tilde{k}}{\sigma_\omega \tilde{\omega}} \right) \frac{\partial \tilde{\omega}}{\partial x_j} \right] - C_{\omega_p} \left(\frac{\tilde{\omega}}{\tilde{k}} \right) \bar{\rho} \widetilde{u_i'' u_j''} \frac{\partial \tilde{u}_i}{\partial x_j} - C_{\omega_d} \bar{\rho}\tilde{\omega}^2 \\ &\quad + \sigma_{cd} \left(\frac{\bar{\rho}}{\tilde{\omega}} \right) \frac{\partial \tilde{k}}{\partial x_j} \frac{\partial \tilde{\omega}}{\partial x_j}\end{aligned}\quad (\text{D22})$$

where the eddy viscosity is given by

$$\mu_t = C_\mu \bar{\rho} \frac{\tilde{k}}{\tilde{\omega}} \quad (\text{D23})$$

and the limited turbulent time scale, $\hat{\omega}$, is defined by the following expression.

$$\hat{\omega} = \text{MAX} \left[\omega, \sigma_{sl} \sqrt{2 \left(\tilde{S}_{ij} - \frac{1}{3} \delta_{ij} \tilde{S}_{kk} \right) \left(\tilde{S}_{ij} - \frac{1}{3} \delta_{ij} \tilde{S}_{kk} \right)} \right] \quad (\text{D24})$$

The closure coefficients associated with this model are defined as

$$\begin{aligned}\frac{1}{\sigma_k} &= 0.6 & \frac{1}{\sigma_\omega} &= 0.5 \\ C_\mu &= 0.09 & C_{k_d} &= 1.0 \\ C_{\omega_d} &= 0.0708 \frac{f_\omega}{C_\mu} & C_{\omega_p} &= \frac{13}{25} \\ \sigma_{sl} &= \frac{7}{8} \left(\frac{C_\mu}{C_{k_d}} \right)^{\frac{1}{2}} & \sigma_{cd} &= \begin{cases} 0 & \frac{\partial \tilde{k}}{\partial x_j} \frac{\partial \tilde{\omega}}{\partial x_j} \leq 0 \\ \frac{C_\mu}{8} & \frac{\partial \tilde{k}}{\partial x_j} \frac{\partial \tilde{\omega}}{\partial x_j} > 0 \end{cases} \\ f_\omega &= \frac{1 + 85 \chi_\omega}{1 + 100 \chi_\omega} & \chi_\omega &= \left(\frac{C_\mu}{0.09} \right)^3 \frac{|\bar{\Omega}_{ij} \bar{\Omega}_{jk} (\tilde{S}_{ki} - \frac{1}{2} \delta_{ki} \frac{\partial \tilde{u}_l}{\partial x_l})|}{\tilde{\omega}^3}\end{aligned}\quad (\text{D25})$$

where it should be noted that the values above reflect the VULCAN-CFD convention that defines ω as (ϵ/k) rather than the $(0.09 \epsilon/k)$ definition used by Wilcox.³⁹

A version of this model that accounts for low Reynolds number effects, while also allowing for improved predictions of laminar to turbulent boundary layer transition, is also available. This variant is identical to the standard model described above, but with the C_μ , C_{k_d} , and C_{ω_p} coefficients (as they appear in Eqs. D22 and D23) modified as follows

$$\begin{aligned}C_\mu^* &= C_\mu \left[\frac{\frac{0.0708}{3} + \frac{Re_t}{6}}{1 + \frac{Re_t}{6}} \right] \\ C_{k_d}^* &= C_{k_d} \left[\frac{0.0708 \left(\frac{100}{27} \right) + \left(\frac{Re_t}{8} \right)^4}{1 + \left(\frac{Re_t}{8} \right)^4} \right] \\ C_{\omega_p}^* &= C_{\omega_p} \left[\frac{\frac{1}{9} + \frac{Re_t}{2.61}}{1 + \frac{Re_t}{2.61}} \right] \left(\frac{C_\mu}{C_\mu^*} \right)\end{aligned}\quad (\text{D26})$$

where Re_t is the turbulence Reynolds number defined by the expression below.

$$Re_t = \frac{C_\mu \bar{\rho} \frac{\tilde{k}}{\tilde{\omega}}}{\mu} \quad (D27)$$

The low Reynolds number corrections also require the following adjustment to the stress limiter coefficient.

$$\sigma_{sl}^* = \sigma_{sl} \left(\frac{C_\mu^*}{C_\mu} \right)^{\frac{1}{2}} \quad (D28)$$

D.5 Gatski and Rumsey 2003 k - ω EAS Model

Nonlinear eddy viscosity models, such as Explicit Algebraic Stress (EAS) closures, can predict certain aspects of turbulent flows that linear (i.e., Boussinesq) models are incapable of capturing. An example is the ability to predict secondary flow structures that arise due to Reynolds stress anisotropies. This flow feature cannot be captured if one assumes a linear relationship between the Reynolds stress and mean strain rate tensors. The computational cost associated with nonlinear eddy viscosity models is only slightly greater than that required for two-equation linear eddy viscosity closures. Hence, models from this class represent a reasonable compromise between linear two-equation formulations and full second-order closures. The EAS model implemented in VULCAN-CFD is the Gatski and Rumsey formulation,⁴⁵ which expresses the Reynolds stress tensor in terms of the mean strain rate and rotation rate tensors via the following relationship

$$\begin{aligned} \bar{\rho} \widetilde{u_i'' u_j''} &= \frac{2}{3} \delta_{ij} \bar{\rho} \tilde{k} - \\ &\mu_t \left(2\tilde{S}_{ij} - \frac{2}{3} \delta_{ij} \tilde{S}_{kk} + 2 \left[a_2 a_4 (\tilde{S}_{ik} \tilde{\Omega}_{kj} - \tilde{\Omega}_{ik} \tilde{S}_{kj}) - a_3 a_4 \left(2\tilde{S}_{ik} \tilde{S}_{kj} - \frac{2}{3} \delta_{ij} \tilde{S}_{kl} \tilde{S}_{lk} \right) \right] \right) \end{aligned} \quad (D29)$$

where the eddy viscosity is given by

$$\mu_t = C_\mu^* \bar{\rho} \frac{\tilde{k}}{\tilde{\omega}} \quad (D30)$$

and the transport equations for k and ω are expressed as shown below.

$$\begin{aligned} \frac{\partial}{\partial t} (\bar{\rho} \tilde{k}) + \frac{\partial}{\partial x_j} (\bar{\rho} \tilde{k} \tilde{u}_j) &= \frac{\partial}{\partial x_j} \left[\left(\mu + \frac{\mu_t}{\sigma_k} \right) \frac{\partial \tilde{k}}{\partial x_j} \right] - \bar{\rho} \widetilde{u_i'' u_j''} \frac{\partial \tilde{u}_i}{\partial x_j} - C_{k_d} \bar{\rho} \tilde{k} \tilde{\omega} \\ \frac{\partial}{\partial t} (\bar{\rho} \tilde{\omega}) + \frac{\partial}{\partial x_j} (\bar{\rho} \tilde{\omega} \tilde{u}_j) &= \frac{\partial}{\partial x_j} \left[\left(\mu + \frac{\mu_t}{\sigma_\omega} \right) \frac{\partial \tilde{\omega}}{\partial x_j} \right] - C_{\omega_p} \left(\frac{\tilde{\omega}}{\tilde{k}} \right) \bar{\rho} \widetilde{u_i'' u_j''} \frac{\partial \tilde{u}_i}{\partial x_j} - C_{\omega_d} \bar{\rho} \tilde{\omega}^2 \end{aligned} \quad (D31)$$

The coefficient, C_μ^* , is governed by the following cubic equation

$$(-C_\mu^*)^3 + p(-C_\mu^*)^2 + q(-C_\mu^*) + r = 0 \quad (D32)$$

where

$$\begin{aligned}
p &= \frac{-(2\gamma_1)}{(2\tilde{S}_{ij}\tilde{S}_{ij})\tau^2\gamma_0} \\
q &= \frac{(\gamma_1^2 - (2\tilde{S}_{ij}\tilde{S}_{ij})\tau^2\gamma_0 a_1 - \frac{1}{3}(2\tilde{S}_{ij}\tilde{S}_{ij})\tau^2 a_3^2 + (2\tilde{\Omega}_{ij}\tilde{\Omega}_{ij})\tau^2 a_2^2)}{[(2\tilde{S}_{ij}\tilde{S}_{ij})\tau^2\gamma_0]^2} \\
r &= \frac{(\gamma_1 a_1)}{[(2\tilde{S}_{ij}\tilde{S}_{ij})\tau^2\gamma_0]^2}
\end{aligned} \tag{D33}$$

and the closure coefficients associated with this model are defined below.

$$\begin{aligned}
\frac{1}{\sigma_k} &= 1.0 & \frac{1}{\sigma_\omega} &= \sqrt{C_\mu} (C_{\omega_d} - C_{\omega_p}) / \kappa^2 \\
C_\mu &= 0.0895 & C_{k_d} &= f_k \\
C_{\omega_d} &= 0.074285 / C_\mu & C_{\omega_p} &= 0.53 \\
f_k &= \begin{cases} 1 & \chi_k \leq 0 \\ \frac{1 + 680 \chi_k^2}{1 + 400 \chi_k^2} & \chi_k > 0 \end{cases} & \chi_k &= \frac{C_\mu^2}{\bar{\omega}^3} \frac{\partial \bar{k}}{\partial x_j} \frac{\partial \bar{\omega}}{\partial x_j} \\
a_1 &= \frac{1.46}{3} & a_2 &= 0.8 \\
a_3 &= 0.375 & a_4 &= \tau / [\gamma_1 + C_\mu^* (2\tilde{S}_{ij}\tilde{S}_{ij})\tau^2\gamma_0] \\
\gamma_0 &= 0.9 & \gamma_1 &= 1.7 + \frac{C_{\epsilon_2} - C_{\epsilon_1}}{C_{\epsilon_1} - 1} \\
C_{\epsilon_1} &= 1.44 & C_{\epsilon_2} &= 1.83 \\
\tau &= \frac{1}{\bar{\omega}} & \kappa &= 0.41
\end{aligned} \tag{D34}$$

The desired root in the cubic expression for C_μ^* is the one with the lowest real component that avoids the degenerate case as $2\tilde{S}_{ij}\tilde{S}_{ij} \rightarrow 0$. An algorithm for determining this root is provided by the following pseudocode.

IF $(2\tilde{S}_{ij}\tilde{S}_{ij})\tau^2 < 1 \times 10^{-6}$ THEN

$$C_\mu^* = \frac{\gamma_1 a_1}{\gamma_1^2 + (2\tilde{\Omega}_{ij}\tilde{\Omega}_{ij})\tau^2 a_2^2}$$

ELSE

$$a = q - \frac{p^2}{3}$$

$$b = \frac{1}{27} (2p^3 - 9pq + 27r)$$

$$c = \frac{b^2}{4} + \frac{a^3}{27}$$

IF $(c > 0)$ THEN

$$t_1 = \left(-\frac{b}{2} + \sqrt{c}\right)^{\frac{1}{3}}$$

$$t_2 = \left(-\frac{b}{2} - \sqrt{c}\right)^{\frac{1}{3}}$$

$$C_\mu^* = -\text{MIN} \left[-\frac{p}{3} + t_1 + t_2, -\frac{p}{3} - \frac{t_1}{2} - \frac{t_2}{2} \right]$$

ELSE

$$\theta = \cos^{-1} \left(\frac{-b/2}{\sqrt{-a^3/27}} \right)$$

$$t_1 = -\frac{p}{3} + 2 \left(-\frac{a}{3}\right)^{\frac{1}{2}} \cos\left(\frac{\theta}{3}\right)$$

$$t_2 = -\frac{p}{3} + 2 \left(-\frac{a}{3}\right)^{\frac{1}{2}} \cos\left(\frac{2\pi}{3} + \frac{\theta}{3}\right)$$

$$t_3 = -\frac{p}{3} + 2 \left(-\frac{a}{3}\right)^{\frac{1}{2}} \cos\left(\frac{4\pi}{3} + \frac{\theta}{3}\right)$$

$$C_\mu^* = -\text{MIN} [t_1, t_2, t_3]$$

END IF

END IF

$$C_\mu^* = \text{MIN} [C_\mu^*, 5.0 \times 10^{-4}]$$

D.6 Wall Functions

An accurate simulation of turbulent wall-bounded flows with standard no-slip surface boundary conditions requires that the grid be clustered to the surface so that the first cell height results in a dimensionless law-of-the-wall coordinate (y^+) value of unity or less. Values much larger than this can result in significant solution inaccuracies and often leads to simulation instabilities. In practice, it is difficult to determine the wall spacing requirements for complex geometries that satisfy this criteria everywhere. Even in situations where the wall

spacing requirements can be determined a priori, the computational cost of numerically resolving the viscous sublayer can be prohibitive. Hence, it is often convenient to avoid the integration of the governing equations through the viscous sublayer by assuming the validity of the Law-of-the-Wall, and forcing the solution at grid points adjacent to the surface to satisfy the log law behavior of turbulent boundary layers. The constitutive relations that are arrived at to enforce this behavior have historically been called “wall functions”.

Traditional wall functions are derived by examining the limiting form of the governing equations as the wall-normal coordinate approaches zero. In this asymptotic limit, the convective terms and the viscous terms not aligned with the wall-normal direction can be neglected, leading to the following simplified equation set for k - ω formulations.

$$\frac{dP}{dy} = 0 \quad (\text{D35})$$

$$\frac{d}{dy} \left[(\mu + \mu_t) \frac{du}{dy} \right] = 0 \quad (\text{D36})$$

$$\frac{d}{dy} \left[\left(\frac{\mu C_p}{Pr} + \frac{\mu_t C_p}{Pr_t} \right) \frac{dT}{dy} + \frac{1}{2} (\mu + \mu_t) \frac{du^2}{dy} \right] = 0 \quad (\text{D37})$$

$$\mu_t \left(\frac{du}{dy} \right)^2 - C_{k_d} \rho k \omega + \frac{d}{dy} \left[\left(\mu + \frac{\mu_t}{\sigma_k} \right) \frac{dk}{dy} \right] = 0 \quad (\text{D38})$$

$$C_{\omega_p} \rho \left(\frac{du}{dy} \right)^2 - C_{\omega_d} \rho \omega^2 + \frac{d}{dy} \left[\left(\mu + \frac{\mu_t}{\sigma_\omega} \right) \frac{d\omega}{dy} \right] = 0 \quad (\text{D39})$$

In these expressions, y represents the wall-normal coordinate, and u represents the streamwise velocity component. To arrive at these equations, it has also been assumed that the chemical composition is frozen from the wall to the first grid point away from the surface (i.e., the wall matching point).

$$\frac{dY_m}{dy} = 0 \quad (\text{D40})$$

If the wall matching point is located within the log layer, then the relationships above can be simplified further by dropping all instances of the molecular viscosity. The use of the log law relationship then provides the information that relates the streamwise velocity to the shear stress, leading to the following standard wall function expressions

$$P = P_w \quad (\text{D41})$$

$$u^* = u_\tau \left[\frac{1}{\kappa} \ln(y^+) + C \right] \quad (\text{D42})$$

$$T = T_w - \left(\frac{Pr_t q_w}{C_p \tau_w} \right) u - \left(\frac{Pr_t}{2 C_p} \right) u^2 \quad (\text{D43})$$

$$k = \left(\frac{\rho_w}{\rho} \right) \left[u_\tau^2 / (C_\mu C_{k_d})^{1/2} \right] \quad (\text{D44})$$

$$\omega = (C_\mu \sqrt{k}) / \left[(C_\mu C_{k_d})^{1/4} \kappa y \right] \quad (\text{D45})$$

where the subscript w represents a surface value, y^+ is the dimensionless wall-normal coordinate,

$$y^+ = \frac{y u_\tau}{\mu/\rho} \quad (\text{D46})$$

u_τ is the friction velocity,

$$u_\tau = \sqrt{\frac{\tau_w}{\rho_w}} \quad (\text{D47})$$

and the quantity u^* is the compressibility corrected velocity defined by the following expression.

$$du^* = \sqrt{\frac{\rho}{\rho_w}} du \quad (\text{D48})$$

The density ratio (ρ/ρ_w) is obtained by combining the ideal gas law with Eqs. D41 and D43, allowing the integration of Eq. D48 to provide the relationship between u^* and u

$$u^* = \frac{1}{A} \left[\sin^{-1} \left(\frac{2A^2 u - B}{\sqrt{B^2 + 4A^2}} \right) + \sin^{-1} \left(\frac{B}{\sqrt{B^2 + 4A^2}} \right) \right] \quad (\text{D49})$$

where

$$A^2 = \frac{Pr_t}{C_p T_w}, \quad B = -\frac{Pr_t q_w}{C_p T_w \tau_w} \quad (\text{D50})$$

close out the modeled expressions.

Solutions obtained using the standard wall functions described above display a high degree of sensitivity to the grid spacing adjacent to the wall. Wilcox⁴⁶ has demonstrated that this sensitivity can be mitigated to a large extent by retaining information from the streamwise pressure gradient. This can be achieved in an efficient fashion by seeking wall function relations that account for the streamwise pressure gradient effect via an asymptotic expansion.^{39,43}

$$u^* = u_\tau \left[\frac{1}{\kappa} \ln(y^+) + C - 1.13 y^+ P^+ + \mathcal{O}(P^+)^2 + \dots \right] \quad (\text{D51})$$

$$k = \left(\frac{\rho_w}{\rho} \right) \left[u_\tau^2 / (C_\mu C_{k_d})^{1/2} \right] \left[1 + 1.16 y^+ P^+ + \mathcal{O}(P^+)^2 + \dots \right] \quad (\text{D52})$$

$$\omega = (C_\mu \sqrt{k}) / \left[(C_\mu C_{k_d})^{1/4} \kappa y \right] \left[1 - 0.30 y^+ P^+ + \mathcal{O}(P^+)^2 + \dots \right] \quad (\text{D53})$$

These expansions have been derived with the assumption that the dimensionless pressure gradient parameter, P^+ ,

$$P^+ \equiv \frac{\mu/\rho}{\rho u_\tau^2} \frac{dP}{dx} \quad (\text{D54})$$

is a small parameter. Simulations of flat plate flows subjected to an adverse pressure gradient (retaining only corrections on the order of P^+) have been shown to reproduce wall-resolved simulation results with the matching point chosen as high as $y^+ = 100$.⁴⁶ It is emphasized that the above relationships have been derived assuming that the matching point resides in the log layer. Simulations of supersonic adiabatic flat plate flows have shown

that the skin friction error (relative to wall-resolved simulations) is a minimum when the matching point is placed near a y^+ of around 30, but the error is less than 5% even when the matching point is chosen as high as y^+ approaching 250.⁴⁶ Errors can become much more substantial if the matching point is chosen too close to the wall (e.g., within the viscous sublayer). VULCAN-CFD addresses this issue by blending the wall function relationships with the known sublayer asymptotic behavior when the wall matching point resides between $1 < y^+ < 10.8$.

D.7 Compressibility Corrections

The use of Favré averages allows incompressible closures (in principle) to be carried over to compressible flows with the effect of compressibility primarily felt through variations in the mean density field. This practice is sufficient for many compressible flow scenarios, but a variety of “compressibility corrections” have been postulated when this assumption proves to be insufficient. One popular correction has been developed to mimic the experimentally observed reduction in free shear layer growth rate as the convective Mach number⁴⁷

$$M_c \equiv \frac{|u_1 - u_2|}{a_1 + a_2} \quad (\text{D55})$$

increases. Here, the quantities u_1, a_1 and u_2, a_2 refer to the freestream velocity and speed of sound on either side of the shear layer. VULCAN-CFD includes an option to enable this class of compressibility correction when a k - ω closure is utilized. The premise behind the correction is to decompose the turbulent dissipation (ϵ) into its solenoidal (vorticity fluctuation variance) and dilatation (divergence of fluctuating velocity field) components. The solenoidal dissipation is the quantity obtained by integrating the standard ϵ equation (or “ ωk ” for k - ω closures), while the dilatation dissipation is modeled in terms of the turbulent Mach number.

$$M_t \equiv \frac{\sqrt{2} \overline{k}}{a} \quad (\text{D56})$$

The functional form for the dilatation dissipation used in VULCAN-CFD is the Wilcox^{39,43} formulation, which has been designed so that the correction has a minimal influence in wall-bounded regions. The model involves the following adjustments to the C_{k_d} and C_{ω_d} coefficients

$$\begin{aligned} C_{k_d}^* &= C_{k_d} [1.0 + \xi^* F(M_t)] \\ C_{\omega_d}^* &= C_{\omega_d} - C_{k_d} \xi^* F(M_t) \end{aligned} \quad (\text{D57})$$

where the constant ξ^* is defined as 1.5 for all of the k - ω closures in VULCAN-CFD except for the Wilcox 2006 model, where it is defined as 2.0. The functional form for $F(M_t)$ is given by the expression

$$F(M_t) = (M_t^2 - M_{t_o}^2) \mathcal{H}(M_t - M_{t_o}) \quad (\text{D58})$$

where \mathcal{H} is the Heaviside step function and $M_{t_o} = 0.25$.

Appendix E

Spatially-Filtered Turbulence Closure Models

Explicit closure models for the spatially-filtered equation set typically vary in complexity from algebraic closures to one-equation models that track the transport of the SGS turbulent kinetic energy. While some have attempted to develop two-equation formulations, this strategy has not been widely adopted due to the natural choice of modeling the subgrid length scale, Δ , as a quantity proportional to the grid spacing.

$$\Delta = (\text{cell volume})^{\frac{1}{3}} \quad \text{or} \quad \text{MAX}[\Delta_x, \Delta_y, \Delta_z] \quad (\text{E1})$$

This observation has led many to consider a class of closures termed Implicit Large Eddy Simulation (ILES), where the inherent numerical diffusion present in the numerical scheme is taken to be sufficient to model the unresolved subgrid terms. This closure maximizes the range of turbulence scales that can be resolved by a given grid, but at the expense of an increased sensitivity to grid resolution (since the filter width cannot be held fixed as the grid is refined). VULCAN-CFD contains options for both static and dynamic algebraic closures, one-equation closures, as well as the option to employ ILES.

E.1 Smagorinsky Model

Smagorinsky⁴⁸ was the first to propose a closure for the subgrid terms. This model utilizes the following functional form for the subgrid viscosity

$$\mu_{sgs} = C_s^2 \bar{\rho} \Delta^2 \sqrt{2\tilde{S}_{ij}\tilde{S}_{ij}} \quad (\text{E2})$$

where \tilde{S}_{ij} is the strain rate tensor of the resolved velocity field. Unfortunately, the closure coefficient, C_s , is far from universal and values used in the literature typically vary between 0.1 and 0.2. Moreover, this functional form does not properly approach zero at the wall for boundary layer flows requiring the use of a damping function to force this behavior.

$$\mu_{sgs} = C_\mu \bar{\rho} \Delta^2 \sqrt{2\tilde{S}_{ij}\tilde{S}_{ij}} \quad (\text{E3})$$

The damping function utilized in VULCAN-CFD is a van Driest form,

$$C_\mu = C_s^2 \left(1.0 - \exp\left[-\frac{y^+}{26}\right] \right)^2, \quad y^+ = \frac{\bar{\rho} y u_\tau}{\mu} \quad (\text{E4})$$

where the friction velocity, $u_\tau = \sqrt{\tau_w/\rho_w}$, is evaluated based on surface shear stress and density values that have been spatially averaged in periodic directions (implying turbulence homogeneity in these directions).

E.2 Vreman Model

Vreman⁴⁹ proposed an algebraic closure that offers several improvements over the classical Smagorinsky model for inhomogeneous turbulent flows. The model is essentially no more

complicated than the Smagorinsky model but is constructed in such a way that its dissipation is relatively small in transitional and near-wall regions. In addition, the model is based on a fundamental realizability inequality for the theoretical subgrid dissipation. This model utilizes the following functional form for the subgrid viscosity

$$\mu_{sgs} = C_\mu \bar{\rho} \sqrt{\frac{B_\beta}{\alpha_{ij}\alpha_{ij}}} \quad (\text{E5})$$

where $C_\mu = 2.5 C_s^2$, α_{ij} is the matrix of filtered velocity field derivatives,

$$\alpha_{ij} = \frac{\partial \bar{u}_j}{\partial x_i} \quad (\text{E6})$$

and B_β is an invariant of the tensor β_{ij} defined by the following expression.

$$B_\beta = \beta_{11}\beta_{22} - \beta_{12}^2 + \beta_{11}\beta_{33} - \beta_{13}^2 + \beta_{22}\beta_{33} - \beta_{23}^2, \quad \beta_{ij} = \sum_{m=1}^3 \Delta_m \alpha_{mi} \alpha_{mj} \quad (\text{E7})$$

In the expression for β_{ij} , the filter width vector components are simply the filter width contributions from each of the coordinate directions. Unlike the standard Smagorinsky model, the Vreman formulation has been shown to display appropriate transitional and near-wall behavior without requiring any ad hoc damping functions. Moreover, reasonable agreement for both mixing layers and boundary layers can be achieved with a single value for the closure coefficient, C_s , which is typically set to the theoretical value (for homogeneous isotropic turbulence) of 1/6 as derived from the Smagorinsky closure.

E.3 Yoshizawa Model

The Yoshizawa model⁵⁰ is a one-equation SGS closure that utilizes the following transport equation for the subgrid turbulent kinetic energy,

$$\frac{\partial}{\partial t} (\bar{\rho} \tilde{k}) + \frac{\partial}{\partial x_j} (\bar{\rho} \tilde{k} \tilde{u}_j) = \frac{\partial}{\partial x_j} \left[\left(\mu + \frac{\mu_{sgs}}{\sigma_k} \right) \frac{\partial \tilde{k}}{\partial x_j} \right] - (\bar{\rho} \widetilde{u_i u_j} - \bar{\rho} \tilde{u}_i \tilde{u}_j) \frac{\partial \tilde{u}_i}{\partial x_j} - C_{k_d} \frac{\bar{\rho} \tilde{k}^{\frac{3}{2}}}{\Delta} \quad (\text{E8})$$

which is used to provide the subgrid velocity scale to the following relationship for the SGS viscosity.

$$\mu_{sgs} = C_\mu \bar{\rho} \sqrt{\tilde{k}} \Delta \quad (\text{E9})$$

The closure coefficients associated with this model are defined as shown below.

$$\frac{1}{\sigma_k} = 2.0 \quad C_\mu = 0.05 \quad C_{k_d} = 1.0 \quad (\text{E10})$$

The principle advantage of one-equation closure models is that they do not explicitly assume a balance of energy (i.e., balance of production and destruction of subgrid energy) implied by simple algebraic models like the Smagorinsky model. Hence, this model has some ability to recover “history” effects (i.e., knowledge of where the flow originated from); a feature that cannot be captured by algebraic closures.

E.4 Dynamic SGS Closures

Germano et al.⁵¹ introduced a significant advancement in SGS modeling by formulating a procedure that allows the closure coefficients to be computed (rather than specified a priori) using scale similarity arguments. The scale similarity assumption allows one to “test-filter” the computationally resolved flow scales using a filter that is larger than the intended filter size to determine the closure coefficient value that minimizes the error (typically represented as an L2 norm) between the output data of the model and the “test-filtered” data. This procedure is formalized through the Germano identity, i.e.,

$$\mathcal{L}_{ij} = \mathcal{T}_{ij} - \tau_{ij} \quad (\text{E11})$$

which relates the resolved stress tensor at the test filter scale, \mathcal{L}_{ij} ,

$$\mathcal{L}_{ij} = \overline{\overline{\rho \tilde{u}_i \tilde{u}_j}} - \frac{\overline{\overline{\rho \tilde{u}_i \tilde{u}_i}}}{\overline{\overline{\rho}}} \quad (\text{E12})$$

to the difference between the SGS stress tensor (model dependent) evaluated at the test filter scale,

$$\mathcal{T}_{ij} = \mathcal{T}_{ij}(\overline{\overline{\rho}}, \overline{\overline{\tilde{u}_i}}, \overline{\overline{\rho \tilde{k}}}, \dots) \quad (\text{E13})$$

and the test filtered SGS stress tensor evaluated at the subgrid scale.

$$\tau_{ij} = \overline{\overline{\rho \tilde{u}_i \tilde{u}_j}} - \overline{\overline{\rho \tilde{u}_i \tilde{u}_i}} \quad (\text{E14})$$

In the expressions above, the second overline denotes the spatial filtering operation at the larger test filter size, $\hat{\Delta}$. Rewriting Eq. E11 in a traceless form,

$$\begin{aligned} \mathcal{L}_{ij} - \frac{1}{3} \delta_{ij} \mathcal{L}_{kk} &= \left(\mathcal{T}_{ij} - \frac{2}{3} \delta_{ij} \overline{\overline{\rho \tilde{k}}} \right) - \left(\tau_{ij} - \frac{2}{3} \delta_{ij} \overline{\overline{\rho \tilde{k}}} \right) \\ \mathcal{L}_{ij}^* &= \mathcal{T}_{ij}^* - \tau_{ij}^* \end{aligned} \quad (\text{E15})$$

and invoking the assumption that the SGS coefficient is constant over the spatial range between the subgrid filter and the test filter sizes, yields the following overdetermined expression for the SGS coefficient

$$\mathcal{L}_{ij}^* = C_\mu \mathcal{M}_{ij}^* \quad (\text{E16})$$

where \mathcal{M}_{ij}^* is defined by the following expression.

$$\mathcal{M}_{ij}^* = \frac{\mathcal{T}_{ij}^* - \tau_{ij}^*}{C_\mu} \quad (\text{E17})$$

Minimizing the error in the L2 norm of this tensor expression results in the following equation for the SGS viscosity coefficient, C_μ .

$$C_\mu = \frac{\mathcal{L}_{ij}^* \mathcal{M}_{ij}^*}{\mathcal{M}_{kl}^* \mathcal{M}_{kl}^*} \quad (\text{E18})$$

In practice, the above expression can result in a large variability in C_μ (even leading to negative values), which may lead to numerical instabilities. In order to mitigate this issue, VULCAN-CFD clips the dynamic SGS coefficient to ensure nonnegative values, along

with the inclusion of options to explicitly smooth the C_μ values spatially. Moreover, if directions of turbulence homogeneity are present, and if the grid block connectivities are full face matching in these directions, then the C_μ values can be spatially averaged in these directions.

Another dynamic procedure, based on a stochastic analysis of the LES equations, has been proposed by Heinz et al.⁵² This formulation results in a dynamic closure model that assumes structural similarity between the Leonard stress tensor and the subgrid stress tensor (as opposed to the structural similarity assumed between the test filter stress and subgrid stress tensors in the Germano formulation).

$$\mathcal{L}_{ij} = -\tau_{ij} \quad (\text{E19})$$

Utilizing the same process and assumptions described above for the Germano formulation yields the following overdetermined expression for the SGS viscosity coefficient

$$\mathcal{L}_{ij}^* = C_\mu \mathcal{H}_{ij}^* \quad (\text{E20})$$

where \mathcal{H}_{ij}^* is defined by the following expression.

$$\mathcal{H}_{ij}^* = \frac{-\tau_{ij}^*}{C_\mu} \quad (\text{E21})$$

Minimizing the error in the L2 norm of this tensor expression results in the following equation for the SGS viscosity coefficient, C_μ .

$$C_\mu = \frac{\mathcal{L}_{ij}^* \mathcal{H}_{ij}^*}{\mathcal{H}_{kl}^* \mathcal{H}_{kl}^*} \quad (\text{E22})$$

This formulation tends to produce considerably less spatial variability in the values for C_μ but does not completely eliminate the numerical instabilities associated with dynamic SGS closures. Hence, the elimination of negative values and some level of smoothing and/or spatial averaging is still often required.

As a final note, one can extend either of these dynamic SGS procedures to any of the modeled SGS terms (e.g., to obtain dynamic values for the subgrid Prandtl and Schmidt numbers). However, these extensions are not yet available in VULCAN-CFD.

Appendix F

Blended RAS/LES Formulation

The blended hybrid RAS/LES methodology framework was designed to enforce a RAS behavior near solid surfaces, and switch to an LES behavior in the outer portion of the boundary layer and free shear regions. Hence, this formulation can be thought of as a wall-modeled LES approach, where RAS is used as the near-wall model. The basic idea is to blend any trusted RAS eddy viscosity with the desired SGS viscosity. Any turbulent transport equation involving a common RAS and SGS property is also blended. In VULCAN-CFD, this framework can be utilized to blend any of the linear $k-\omega$ models with any static SGS closure model (including ILES). The blended effective turbulent viscosity is obtained by the following expression,

$$\text{Hybrid RAS/SGS viscosity} = (F) [\text{RAS viscosity}] + (1 - F) [\text{SGS viscosity}] \quad (\text{F1})$$

and if the SGS closure involves a transport equation for the SGS kinetic energy, then the turbulent kinetic energy transport equations are also blended, i.e.,

$$\text{Hybrid RAS/SGS k-equation} = (F) [\text{RAS k-equation}] + (1 - F) [\text{SGS k-equation}] \quad (\text{F2})$$

where F is a blending function that varies between 0 and 1. Note that the transport equation for the RAS specific dissipation rate (ω) does not have an SGS counterpart. Hence, the blending is not applied to this equation, and all of the terms in this equation that involve the eddy viscosity are evaluated based on RAS relationships.

A variety of functional relationships have been devised to control the blending of RAS and LES. The blending in VULCAN-CFD is parameterized by the ratio of the wall distance d to a modeled form of the Taylor microscale (λ)

$$F = \frac{1}{2} \left\{ 1 - \tanh \left[5 \left(\frac{\kappa}{\sqrt{C_\mu}} \eta^2 - 1 \right) - \tanh^{-1}(0.98) \right] \right\}$$
$$\eta = \frac{d}{\alpha \lambda}, \quad \lambda = \sqrt{\frac{\mu}{C_\mu \rho \omega}} \quad (\text{F3})$$

where κ is the von Karman constant (0.41), C_μ is 0.09, α is a user defined model constant, and the factor $\tanh^{-1}(0.98)$ is used to force the balancing position of F (i.e., the position where $\kappa \eta^2 = \sqrt{C_\mu}$) to 0.99. The value chosen for α provides control over the d^+ position where the average LES to RAS transition point (defined as $F = 0.99$) occurs. If resolved LES content is desired for attached boundary layers, then this constant should be specified so that the transition position occurs in the region where the boundary layer wake law starts to deviate from the log law. If the transition point is enforced at a lower d^+ value that is well within the log law region, a dual log layer appears (an effect often referred to as the log layer mismatch).⁵³ Conversely, if the transition point is enforced at a d^+ value that extends well into the wake region, then the level of resolved turbulent content will be reduced. Details on a procedure to analytically determine the value for α that corresponds to a target d^+ value is described by Choi et al.¹⁷.

Appendix G

Improved Delayed Detached Eddy Simulation

The Improved Delayed Detached Eddy Simulation (IDDES) formulation¹⁹ incorporates two major enhancements to the original DES method. The first enhancement led to the DDES (Delayed Detached Eddy Simulation) formulation which sought to prevent the switch from RAS to LES mode within attached boundary layers due solely to the specifics of the grid design. This desirement was realized by altering the DES length scale to incorporate a flow dependent shielding function that maintains the RAS length scale in attached boundary layer flow regions

$$\hat{l}_{DDES} = \tilde{l} - f_d \text{MAX} [0, \tilde{l} - \Delta_{DES}] \quad (\text{G1})$$

where the shielding function, f_d , is defined as

$$f_d = 1 - \tanh \left[\left(C_{f_d} r_d \right)^3 \right], \quad r_d = \frac{\mu + \mu_t}{\bar{\rho} (\kappa d)^2 \text{MAX} \left[\sqrt{\frac{\partial u_i}{\partial x_j} \frac{\partial u_i}{\partial x_j}}, 10^{-10} \right]} \quad (\text{G2})$$

and $C_{f_d} = 8$. The argument r_d is close to unity in the sublayer and logarithmic portions of the boundary layer, and asymptotes to zero as the edge of the boundary layer is approached. As a result, f_d is essentially zero until the defect layer is encountered and rapidly approaches unity when $r_d \ll 1$. The second enhancement was the introduction of a wall-modeled LES functionality. In general, the IDDES formulation provides a wall-modeled LES response if resolved turbulent content is supplied as an inflow (or initial) condition, and resorts to a DDES response (as described above) otherwise.

The wall-modeled LES branch is intended to be active only when the inflow conditions include resolved turbulent content, and the grid is fine enough to at least resolve the largest energy containing boundary layer eddies. This branch uses the following length scale definition

$$\hat{l}_{WMLES} = f_\beta (1 + f_e) \tilde{l} + (1 - f_\beta) \Delta_{DES} \quad (\text{G3})$$

where the empirical blending function, f_β , is formulated as shown below.

$$f_\beta = \text{MIN} \left[2 \exp(-9\alpha^2), 1 \right], \quad \alpha = 0.25 - \frac{d}{\Delta_{max}} \quad (\text{G4})$$

This blending function varies from 0 (LES mode) to 1 (RAS mode) and provides a rapid switch between these extremes when the wall distance is between $0.5 \Delta_{max}$ and Δ_{max} . The second empirical function, f_e , is meant to prevent an excessive reduction of the RAS Reynolds stresses in the vicinity of the RAS/LES interface. This function was designed to address the log layer mismatch that plagues hybrid RAS/LES models and takes on the following form

$$f_e = \text{MAX} [(f_{e1} - 1), 0] \Psi f_{e2} \quad (\text{G5})$$

where the relationships for f_{e1} and f_{e2} are provided below.

$$f_{e1} = \begin{cases} 2 \exp(-11.09 \alpha^2) & \alpha \geq 0 \\ 2 \exp(-9.0 \alpha^2) & \alpha < 0 \end{cases} \quad (\text{G6})$$

$$f_{e_2} = 1 - \text{MAX} \left[\tanh \left\{ \left(c_t^2 r_{d_t} \right)^3 \right\}, \tanh \left\{ \left(c_l^2 r_{d_l} \right)^{10} \right\} \right] \quad (\text{G7})$$

The quantity Ψ is the low Reynolds number correction introduced in the definition of Δ_{DES} , and r_{d_t} and r_{d_l} are the turbulent and laminar portions of the r_d parameter defined previously. The constants c_t and c_l are meant to ensure that the function f_{e_2} is virtually zero when either r_{d_t} or r_{d_l} is close to 1.0. The appropriate values for these constants are dependent on the specific RAS model utilized. Based on fully developed channel flow simulations, Shur et al.¹⁹ determined that $c_t=1.63$ and $c_l=3.55$ worked well with the Spalart Allmaras model, while $c_t=1.87$ and $c_l=5.0$ worked well with the Menter SST model. VULCAN-CFD currently uses these latter values for all two-equation DES formulations.

The DDES (Eq. G1) and WMLES (Eq. G3) length scales, as written above, cannot easily be blended to ensure that the desired branch is obtained depending on the existence of resolved turbulent content in the boundary layer. However, this desirement is possible with a modified DDES length scale expression of the form

$$\hat{l}_{DDES} = \tilde{f}_d \tilde{l} + (1 - \tilde{f}_d) \Delta_{DES} \quad (\text{G8})$$

where the expression for the blending function, \tilde{f}_d , is shown below.

$$\tilde{f}_d = \text{MAX} \left[1 - f_{d_t}, f_\beta \right], \quad f_{d_t} = 1 - \tanh \left[\left(C_{f_d} r_{d_t} \right)^3 \right] \quad (\text{G9})$$

This essentially equivalent functional replacement for the DDES length scale allows the blending of the DDES and WMLES length scale definitions to be realized via the following expression.

$$\hat{l} = \tilde{f}_d (1 + f_e) \tilde{l} + (1 - \tilde{f}_d) \Delta_{DES} \quad (\text{G10})$$

The hybrid length scale given by Eq. G10 provides the desired WMLES behavior for simulations that contain resolved turbulent content within the boundary layer (since $r_{d_t} \ll 1 \Rightarrow f_{d_t} \approx 1$ so that $\tilde{f}_d = f_\beta$). Conversely, a simulation without resolved turbulence within the boundary layer leads to $f_e \approx 0$ and $f_{d_t} \approx 0 \Rightarrow \tilde{f}_d = 1$.

The DES filter width was also modified in the IDDES formulation to explicitly include the wall distance, d .

$$\Delta_{DES} = \text{MIN} \{ \text{MAX} [C_w d, C_w \Delta_{max}, \Delta_n], \Delta_{max} \} \quad (\text{G11})$$

The quantity Δ_n is the grid spacing in the wall normal direction, which is somewhat ambiguous for complex geometries with multiple walls. VULCAN-CFD evaluates this quantity by averaging the cell center values of the wall distance to grid nodes, allowing an effective “wall-normal” grid spacing to be computed as the difference between the maximum and minimum nodal values for each grid cell. The value of C_w was arrived at based on simulations of fully developed channel flow and taken to be 0.15.

Appendix H

Bleed Models

Two formulations are available in VULCAN-CFD to empirically model the boundary layer effusion process. Figure H1 provides a pictorial representation of the various parameters required to define the bleed/blowing processes.

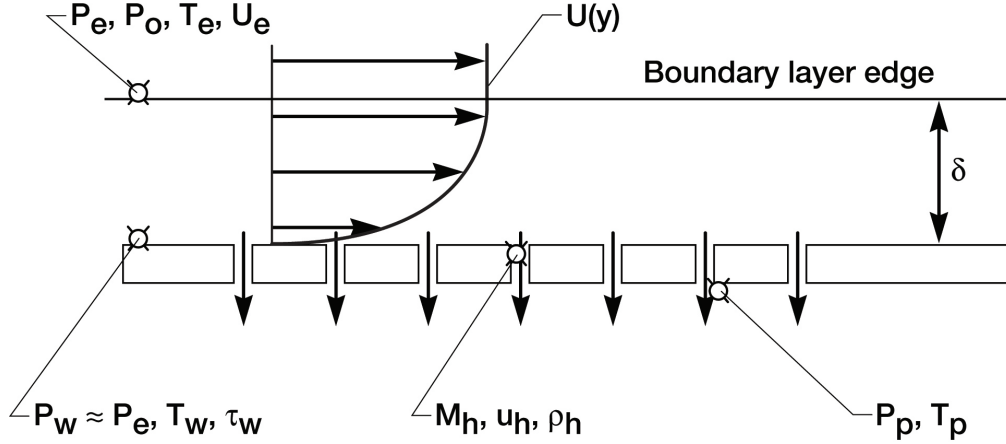


Figure H1: Schematic of effusion through a porous plate.

H.1 Doerffer/Bohning Model

The bleed model of Doerffer and Bohning²¹ is described by the expressions shown below.

$$\text{If } (P_p \geq P_w) : \quad P_p - P_w = P_p \left[\frac{M_h}{1.2} \right]^{0.55} \quad (\text{H1})$$

$$\text{If } (P_w > P_p) : \quad P_w - P_p = P_w \left[\left(\frac{M_h}{1.2} \right)^{0.55} + 25 M_h^{0.55} (C_{f,h} M_h)^{1.52} \right] \quad (\text{H2})$$

These equations define the relation between the pressure drop across the porous plate and the effective Mach number of the flow through the bleed orifices. The functional form of the Doerffer/Bohning effusion model depends on the magnitude of the plenum pressure relative to the wall pressure. When the plenum pressure is greater than the local wall pressure (Eq. H1), the flow is drawn out of the bleed plenum and into the boundary layer. Boundary layer bleed, on the other hand, results when the local surface pressure exceeds the plenum pressure (Eq. H2). Doerffer and Bohning found a “blockage” effect when bleeding flow from the boundary layer into the plenum that was not present when flow effused from the plenum into the boundary layer. They theorized that the “blockage” effect was the result of the shear force present at the entrance of the bleed orifices. To account for this effect, a term that depends on the surface shear stress (normalized by the dynamic pressure of the

bleed orifice)

$$C_{f,h} \equiv \frac{\tau_w}{0.5 \rho_h u_h^2} = \frac{2 \tau_w}{\gamma P_h M_h^2} = \frac{2 \tau_w \left(1 + \frac{\gamma-1}{2} M_h^2\right)^{\frac{\gamma}{\gamma-1}}}{\gamma P_w M_h^2} \quad (\text{H3})$$

was added to the formulation. Equations H1, H2, and H3 reveal that the effective hole Mach number (M_h), is solely a function of the plenum pressure (P_p), surface pressure (P_w), and the surface shear stress (τ_w). Note that the surface shear stress included in this formulation is intended to be the value associated with the approach flow upstream of the porous plate.

The mass flow rate through the bleed orifices of a given cell interface can be expressed as

$$\dot{m}_h = P_o \Phi_{aero} A_{cell} M_h \left(\frac{\gamma}{RT_o}\right)^{\frac{1}{2}} \left(1 + \frac{\gamma-1}{2} M_h^2\right)^{\frac{\gamma+1}{2(1-\gamma)}} \quad (\text{H4})$$

where P_o and T_o are either taken as the wall pressure and temperature (if $P_w > P_p$), or the plenum pressure and temperature (if $P_p \geq P_w$). An important aspect of this effusion model is the ‘‘aerodynamic’’ porosity (Φ_{aero}) that appears in Eq. H4. Doerffer and Bohning performed static transpiration tests on 22 different porous plates with geometrical porosities ranging from 2% to 26.6%, and found that bleed plates with identical geometrical porosities can result in quite different ‘‘aerodynamic’’ porosities. Hence, the length to diameter ratio as well as the quality of the drilled holes influenced the ‘‘aerodynamic’’ porosity. Based on the 22 plates tested by Doerffer and Bohning²¹, the following empirical fit to the data was formulated,

$$\frac{P_w - P_p}{P_w} = 0.063 \left(\frac{\dot{m}}{A_{aero}}\right)^2 \quad (\text{H5})$$

which relates the ‘‘aerodynamic’’ hole area to the normalized pressure drop across the porous plate and the total effused flow rate. The ‘‘aerodynamic’’ porosity is then obtained by dividing A_{aero} by the total porous plate area. The above formula (Eq. H5) applies to static transpiration tests that bleed air into the plenum (as shown in Fig. H1). The plenum and wall pressures would be swapped in Eq. H5 for static tests that instead effused air out of the plenum.

The implementation of the Doerffer/Bohning model is summarized as follows:

- At a given surface cell interface, Eq. H1 (or H2) is evaluated to determine the effective hole Mach number given the surface pressure, bleed plenum pressure, and surface shear stress (if $P_w > P_p$).
- The remaining bleed hole properties are evaluated given M_h and either P_w and T_w (if $P_w > P_p$), or P_p and T_p (if $P_p \geq P_w$).
- Eq. H4 is evaluated to obtain the local effusion rate at the surface cell interface given P_o , T_o , M_h , and A_{aero} (either estimated or obtained from static porous plate tests).
- The porous plate hole properties together with \dot{m}_h are then used to evaluate the effusion source terms.

H.2 Slater Model

The bleed model developed by Slater²² is based on a parametrization of the bleed physics that uses the concept of the sonic flow coefficient (Q_{sonic}), defined via the following relation.

$$\dot{m}_{bleed} = Q_{sonic} \dot{m}_{sonic} \quad (H6)$$

Q_{sonic} is a parameter that essentially measures the effectiveness of the bleed process, and its value must be obtained from some external means (e.g., measurements). A sample set of Q_{sonic} values derived from measurements⁵⁴ at four Mach number conditions is given in Fig. H2. For a calorically perfect gas, the mass flow rate (\dot{m}) can be recast into the form shown below.

$$\dot{m} = P_o \Phi A_{cell} M \left(\frac{\gamma}{RT_o} \right)^{\frac{1}{2}} \left(1 + \frac{\gamma - 1}{2} M^2 \right)^{\frac{\gamma + 1}{2(1 - \gamma)}} \quad (H7)$$

The reference bleed flow rate (\dot{m}_{sonic}), defined as an isentropic sonic flow condition through the bleed holes, is obtained from this expression by setting the Mach number to one.

$$\dot{m}_{sonic} = P_o \Phi A_{cell} \left(\frac{\gamma}{RT_o} \right)^{\frac{1}{2}} \left(\frac{\gamma + 1}{2} \right)^{\frac{\gamma + 1}{2(1 - \gamma)}} \quad (H8)$$

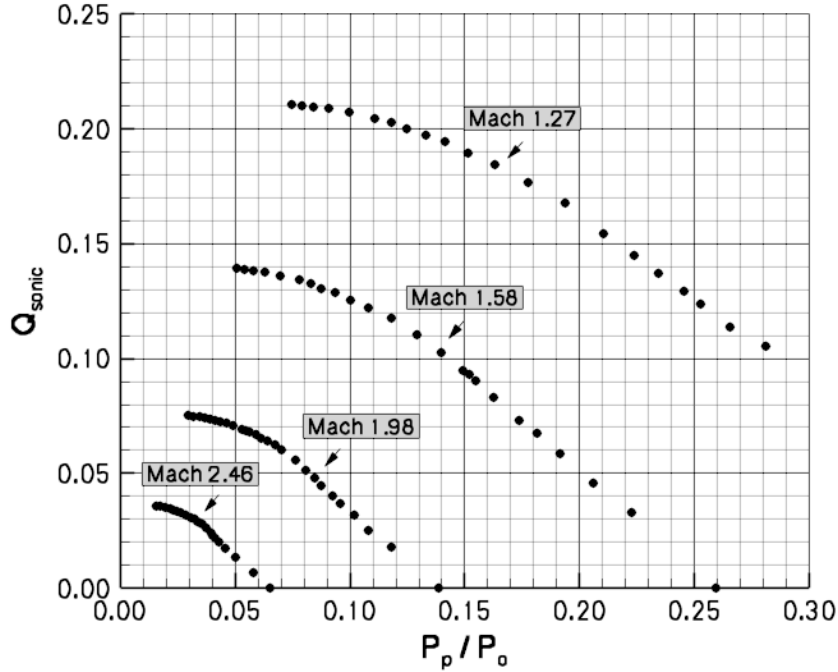


Figure H2: Sonic coefficient data plotted against plenum to total pressure ratio.

Earlier versions of bleed models based on this framework evaluated \dot{m}_{sonic} using boundary layer edge values for total pressure (P_o) and total temperature (T_o), along with a table look-up procedure to extract measured Q_{sonic} values (from curves similar to that given in Fig. H2) given the bleed plenum pressure and boundary layer edge values for Mach number and total pressure. However, the extraction of boundary layer edge conditions is at best a

cumbersome process for a CFD solver, and at worst may not be well defined depending on the complexity of the flow field. The Slater model addresses this issue by introducing a different reference value for \dot{m}_{bleed} that is based on surface properties rather than boundary layer edge conditions.

$$\dot{m}_{sonic}^* = P_w \Phi A_{cell} \left(\frac{\gamma}{RT_w} \right)^{\frac{1}{2}} \left(\frac{\gamma + 1}{2} \right)^{\frac{\gamma+1}{2(1-\gamma)}} \quad (\text{H9})$$

A surface sonic flow coefficient is also defined in a manner analogous to Eq. H6.

$$\dot{m}_{bleed} = Q_{sonic}^* \dot{m}_{sonic}^* \quad (\text{H10})$$

An evaluation of Eqs. H6, H8, H9, and H10 shows that Q_{sonic}^* is related to Q_{sonic} via the following expression.

$$Q_{sonic}^* = Q_{sonic} \left(\frac{P_o}{P_w} \right) \left(\frac{T_w}{T_o} \right)^{\frac{1}{2}} \quad (\text{H11})$$

To simplify the scaling, Slater assumed that the edge pressure is imposed through the boundary layer (standard boundary layer approximation) along with the assumption of a near unity temperature recovery factor.

$$\frac{P_o}{P_w} \approx \frac{P_o}{P_e} = \left(1 + \frac{\gamma - 1}{2} M_e^2 \right)^{\frac{\gamma}{\gamma-1}} \quad (\text{H12})$$

$$\frac{T_w}{T_o} \approx 1.0 \quad (\text{H13})$$

With this simplification, the final scaling of Q_{sonic} and $\frac{P_p}{P_o}$ (i.e., the independent and dependent variables in Fig. H2) reduces to the expressions provided below.

$$Q_{sonic}^* = Q_{sonic} \left(\frac{P_o}{P_w} \right) \quad (\text{H14})$$

$$\frac{P_p}{P_w} = \frac{P_p}{P_o} \left(\frac{P_o}{P_w} \right) \quad (\text{H15})$$

The above scaling results in the surface sonic flow coefficient data shown in Fig. H3. This scaling collapses the separate curves in Fig. H2 for each Mach number, effectively removing Mach number from the parametrization. Slater fit the following quadratic curve to the data presented in Fig. H3.

$$Q_{sonic}^* = 0.59799735 + 0.03069346 \left(\frac{P_p}{P_w} \right) - 0.59361420 \left(\frac{P_p}{P_w} \right)^2 \quad (\text{H16})$$

The implementation of the Slater model is summarized as follows:

- Eq. H16 is evaluated to obtain Q_{sonic}^* at the surface cell interface given the surface pressure and the bleed plenum pressure.
- Eq. H9 is evaluated to obtain \dot{m}_{sonic} at the surface cell interface given the surface pressure and temperature.

- Eq. H10 is evaluated to determine the $\dot{m}_{bleed} = \dot{m}_h$ required to evaluate the effusion source terms.
- Eq. H7 is used to determine the effective Mach number in the bleed holes ($M = M_h$):
 - If Q_{sonic}^* is positive (i.e., flow is drawn into the plenum), then Eq. H7 is evaluated with $P_o = P_w$ and $T_o = T_w$.
 - If Q_{sonic}^* is negative (i.e., flow is drawn out of the plenum), then Eq. H7 is evaluated with $P_o = P_p$ and $T_o = T_p$.
- The remaining bleed hole properties are evaluated given P_o , T_o , and M_h .

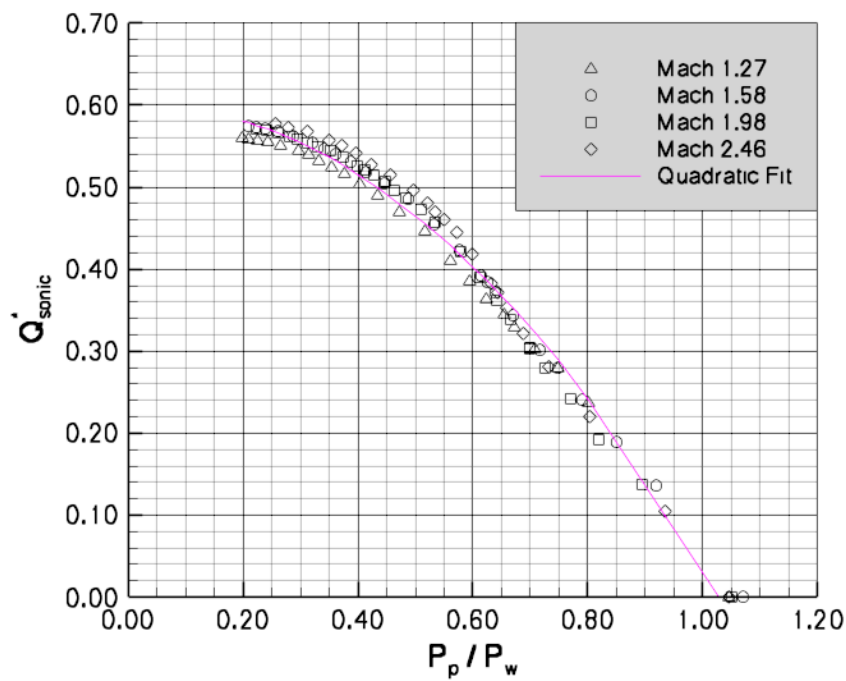


Figure H3: Surface sonic coefficient data plotted against plenum to surface pressure ratio.

Appendix I

Conserved Flux Method Data Reduction

The data reduction process for the conserved Mass/Momentum/Energy (CMME) and Mass/Energy/Entropy (CMES) formulations results in a nonlinear system of coupled equations that require some knowledge of the flow physics to determine the appropriate roots to extract. The decision making process used for each approach is described in the subsections below.

I.1 CMME Method Data Reduction Details

The uniform flow properties that satisfy the integral flux relations for mass, momentum, and energy conservation can be expressed in the following form.

$$f_{mass}^m = [\rho (\vec{v} \cdot \vec{n}) \mathbf{Y}_m] \mathbf{A} \quad (\text{I1a})$$

$$\vec{f}_{momentum} = [\rho (\vec{v} \cdot \vec{n}) \vec{v} + \mathbf{P} \vec{n}] \mathbf{A} \quad (\text{I1b})$$

$$f_{energy} = [\rho (\vec{v} \cdot \vec{n}) \mathbf{h}_o] \mathbf{A} \quad (\text{I1c})$$

The introduction of the total mass flux, \dot{m} ,

$$\dot{m} = \sum_{m=1}^{ns} f_{mass}^m \quad (\text{I2})$$

allows these relations to be recast to the form shown below.

$$f_{mass}^m = \dot{m} \mathbf{Y}_m \quad (\text{I3a})$$

$$\vec{f}_{momentum} = \dot{m} \vec{v} + \mathbf{P} \vec{n} \mathbf{A} \quad (\text{I3b})$$

$$f_{energy} = \dot{m} \mathbf{h}_o \quad (\text{I3c})$$

The mass expression provides an explicit relationship for the uniform composition variables,

$$\mathbf{Y}_m = \frac{f_{mass}^m}{\dot{m}} \quad (\text{I4})$$

and the energy expression provides a direct relationship for the uniform total enthalpy.

$$\mathbf{h}_o = \frac{f_{energy}}{\dot{m}} = \mathbf{h}(\mathbf{T}, \mathbf{Y}_m) + \frac{1}{2} (\vec{v} \cdot \vec{v}) \quad (\text{I5})$$

The momentum expression can be rearranged to yield an expression for the velocity vector,

$$\vec{v} = \frac{\vec{f}_{momentum} - \mathbf{P} \vec{n} \mathbf{A}}{\dot{m}} \quad (\text{I6})$$

which can be simplified to a scalar equation by taking the dot product of this vector with the unit normal (\vec{n}),

$$\vec{v} \cdot \vec{n} = \frac{f_{momentum} - \mathbf{P} \mathbf{A}}{\dot{m}} \quad (\text{I7})$$

where $f_{momentum}$ is defined by the following expression.

$$f_{momentum} \equiv (\vec{f}_{momentum} \cdot \vec{n}) \quad (I8)$$

Further manipulations are possible with the introduction of the equation of state,

$$\mathbf{P} = \rho \mathbf{RT} = \frac{\dot{m} \mathbf{RT}}{(\vec{v} \cdot \vec{n}) \mathbf{A}} \quad (I9)$$

resulting in the following relationship for $(\vec{v} \cdot \vec{n})$.

$$\vec{v} \cdot \vec{n} = \frac{f_{momentum} - \mathbf{PA}}{\dot{m}} = \frac{f_{momentum}}{\dot{m}} - \frac{\mathbf{RT}}{(\vec{v} \cdot \vec{n})} \quad (I10)$$

This equation is quadratic with respect to $(\vec{v} \cdot \vec{n})$, hence the quadratic formula can be used to obtain a closed form solution for $\vec{v} \cdot \vec{n}$.

$$\vec{v} \cdot \vec{n} = \frac{f_{momentum}/\dot{m} \pm [(f_{momentum}/\dot{m})^2 - 4\mathbf{RT}]^{\frac{1}{2}}}{2} \quad (I11)$$

Equations I4, I6, I9 and I11 can then be substituted into Eq. I5 to yield a single expression with static temperature as the only unknown.

$$F(T) = 0 = \mathbf{h}(\mathbf{T}, \mathbf{Y}_m) + \frac{1}{2} (\vec{v} \cdot \vec{v}) - \frac{f_{energy}}{\dot{m}} \quad (I12)$$

This function has the general shape displayed in Fig. I1.

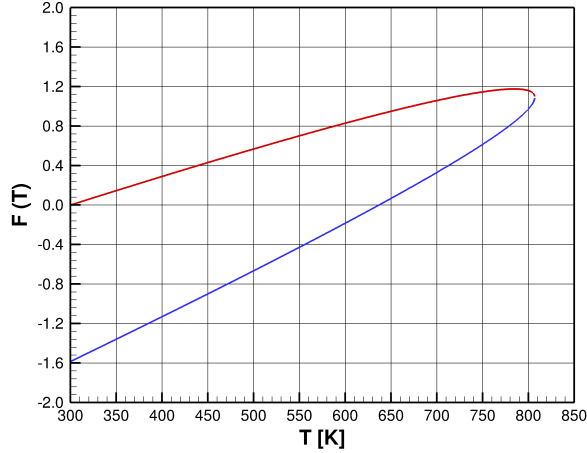


Figure I1: CMME function (colors denote the two branches of Eq. I11).

In principle, any root solving algorithm can be used to solve for the static temperature in Eq. I12. However, there may be two temperature values that satisfy $F(T) = 0$, requiring a method to choose the most appropriate one. Two bisection solves can be employed to determine each temperature that satisfies $F(T) = 0$. The first bisection procedure finds any root (or roots) bounded between T_{min} and T_{max} on the upper (red) portion of the curve,

corresponding to values obtained by choosing the “-” sign in Eq. I11. The second bisection procedure finds the root (if it exists) bounded between T_{min} and T_{max} on the lower (blue) portion of the curve, representing the values obtained when choosing the “+” sign in Eq. I11. T_{max} is the temperature that forces the discriminant of Eq. I11 to be zero, i.e.,

$$\mathbf{T} = \frac{(f_{momentum}/\dot{m})^2}{4\mathbf{R}} \quad (\text{I13})$$

and T_{min} can be taken as either zero, or the lower temperature bound given for the polynomial fits of the thermodynamic data. The temperature value that is retained is the solution that yields a Mach number that lies closest to the mass flux weighted Mach number. As a final note, one may be tempted to assume that the red portion of Fig. II corresponds to only supersonic solutions of $F(T) = 0$, while the blue curve corresponds to the subsonic solutions. However, a careful examination of Eq. I11 reveals that this is not necessarily the case. The Mach number (based on $\vec{\mathbf{v}} \cdot \vec{\mathbf{n}}$) that appears when the discriminant of Eq. I11 vanishes corresponds to a value of $\gamma^{-0.5}$, where γ is the ratio of specific heats. Hence, there is a small range of potential subsonic roots that reside on the red portion of the curve that must be considered when extracting all possible roots for this equation.

I.2 CMES Method Data Reduction Details

The uniform flow properties that satisfy the integral flux relations for mass, energy, and entropy conservation can be expressed in the following form.

$$f_{mass}^m = [\rho (\vec{\mathbf{v}} \cdot \vec{\mathbf{n}}) \mathbf{Y}_m] \mathbf{A} \quad (\text{I14a})$$

$$f_{energy} = [\rho (\vec{\mathbf{v}} \cdot \vec{\mathbf{n}}) \mathbf{h}_o] \mathbf{A} \quad (\text{I14b})$$

$$f_{entropy} = [\rho (\vec{\mathbf{v}} \cdot \vec{\mathbf{n}}) \mathbf{s}] \mathbf{A} \quad (\text{I14c})$$

The introduction of the total mass flux, \dot{m} ,

$$\dot{m} = \sum_{m=1}^{ns} f_{mass}^m \quad (\text{I15})$$

allows these relations to be recast as

$$f_{mass}^m = \dot{m} \mathbf{Y}_m \quad (\text{I16a})$$

$$f_{energy} = \dot{m} \mathbf{h}_o \quad (\text{I16b})$$

$$f_{entropy} = \dot{m} \mathbf{s}(\mathbf{T}, \mathbf{P}, \mathbf{Y}_m) \quad (\text{I16c})$$

leading to explicit relationships for the uniform composition variables, total enthalpy, and entropy. If the unit normal is defined to be aligned with the velocity vector (i.e., $\vec{\mathbf{n}} = \vec{\mathbf{v}}/|\vec{\mathbf{v}}|$), then

$$(\vec{\mathbf{v}} \cdot \vec{\mathbf{n}}) = \sqrt{\vec{\mathbf{v}} \cdot \vec{\mathbf{v}}} \quad (\text{I17})$$

allowing $(\vec{\mathbf{v}} \cdot \vec{\mathbf{n}})$ to be extracted from the definition of total enthalpy.

$$(\vec{\mathbf{v}} \cdot \vec{\mathbf{n}}) = [2 (\mathbf{h}_o - \mathbf{h}(\mathbf{T}, \mathbf{Y}_m))]^{\frac{1}{2}} \quad (\text{I18})$$

It should be noted that the velocity vector is not present in the equations that govern the CMES method. Therefore, it must be supplied by some other means (e.g., by mass flux weighting the velocity components) to define the unit normal. Finally, an expression for the pressure is obtained by combining the equation of state with the total mass flux.

$$\mathbf{P} = \rho \mathbf{R} \mathbf{T} = \frac{\dot{m} \mathbf{R} \mathbf{T}}{(\vec{\mathbf{v}} \cdot \vec{\mathbf{n}}) \mathbf{A}} \quad (\text{I19})$$

Equations I16, I17, I18, and I19 can be combined to yield a single expression with static temperature as the only unknown. For a calorically perfect gas, the resulting function can be expressed in the form shown below.

$$F(T) = 0 = \left[\frac{f_{entropy}}{\dot{m}} - s_{ref} \right] - \left[\frac{\gamma R}{\gamma - 1} \ln \left(\frac{\mathbf{T}}{\mathbf{T}_{ref}} \right) - R \ln \left(\frac{\mathbf{P}}{\mathbf{P}_{ref}} \right) \right] \quad (\text{I20})$$

This function has the general shape displayed in Fig. I2, which shows that two values of temperature will satisfy $F(T) = 0$. One of the roots results in a solution for subsonic flow (blue curve), and the other yields a solution for supersonic flow (red curve). Two bisection solves can be employed to determine each temperature value that satisfies $F(T) = 0$. The first bisection procedure finds the root that is bounded between T_{min} and the temperature at the sonic point, and the second finds the root that is bounded between the temperature at the sonic point and the stagnation temperature. The stagnation temperature is obtained from the solution of

$$\mathbf{h}_o(\mathbf{T}_o, \mathbf{Y}_m) = 0 \quad (\text{I21})$$

and the sonic temperature is the temperature that satisfies the following relationship.

$$\gamma(\mathbf{T}, \mathbf{Y}_m) \mathbf{R} \mathbf{T} = (\vec{\mathbf{v}} \cdot \vec{\mathbf{n}})^2 \quad (\text{I22})$$

T_{min} can be taken as either zero, or the lower temperature bound given for the polynomial fits of the thermodynamic data. If two roots are found, the root that is retained is the one that yields a Mach number closest to the mass flux weighted Mach number.

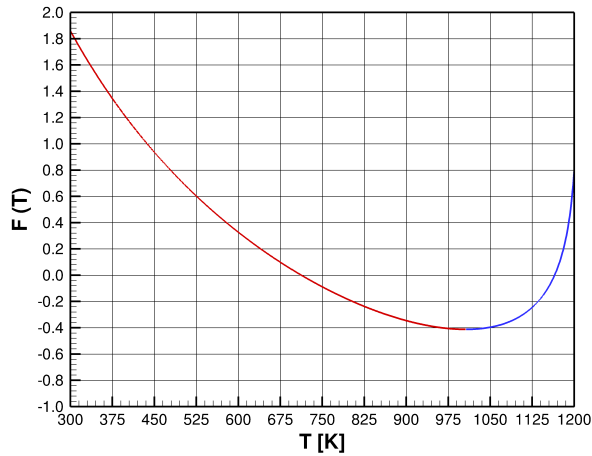


Figure I2: CMES function (colors denote subsonic and supersonic branches of Eq. I20).

REPORT DOCUMENTATION PAGE

*Form Approved
OMB No. 0704-0188*

The public reporting burden for this collection of information is estimated to average 1 hour per response, including the time for reviewing instructions, searching existing data sources, gathering and maintaining the data needed, and completing and reviewing the collection of information. Send comments regarding this burden estimate or any other aspect of this collection of information, including suggestions for reducing this burden, to Department of Defense, Washington Headquarters Services, Directorate for Information Operations and Reports (0704-0188), 1215 Jefferson Davis Highway, Suite 1204, Arlington, VA 22202-4302. Respondents should be aware that notwithstanding any other provision of law, no person shall be subject to any penalty for failing to comply with a collection of information if it does not display a currently valid OMB control number.
PLEASE DO NOT RETURN YOUR FORM TO THE ABOVE ADDRESS.

1. REPORT DATE (DD-MM-YYYY) 01-04-2020		2. REPORT TYPE Technical Memorandum		3. DATES COVERED (From - To)	
4. TITLE AND SUBTITLE VULCAN-CFD Theory Manual: Ver. 7.1.0				5a. CONTRACT NUMBER	
				5b. GRANT NUMBER	
				5c. PROGRAM ELEMENT NUMBER	
6. AUTHOR(S) Baurle, R. A., White, J. A., Drozda, T. G., and Norris, A. T.				5d. PROJECT NUMBER	
				5e. TASK NUMBER	
				5f. WORK UNIT NUMBER 147016.02.07.05.03	
7. PERFORMING ORGANIZATION NAME(S) AND ADDRESS(ES) NASA Langley Research Center Hampton, Virginia 23681-2199				8. PERFORMING ORGANIZATION REPORT NUMBER	
9. SPONSORING/MONITORING AGENCY NAME(S) AND ADDRESS(ES) National Aeronautics and Space Administration Washington, DC 20546-0001				10. SPONSOR/MONITOR'S ACRONYM(S) NASA	
				11. SPONSOR/MONITOR'S REPORT NUMBER(S) NASA/TM-2020-5000766	
12. DISTRIBUTION/AVAILABILITY STATEMENT Unclassified-Unlimited Subject Category 02 Availability: NASA STI Program (757) 864-9658					
13. SUPPLEMENTARY NOTES An electronic version can be found at http://ntrs.nasa.gov .					
14. ABSTRACT VULCAN-CFD offers a comprehensive set of capabilities to enable the simulation of continuum flowfields from subsonic to hypersonic conditions. The governing equations that are employed include allowances for both chemical and thermal nonequilibrium processes, coupled with a wide variety of turbulence models for both Reynolds-averaged and large eddy simulations. Simulations can be performed using structured multiblock meshes or fully unstructured meshes. A parabolic (i.e., space-marching) treatment can also be used for any subset of a structured mesh that can accommodate this solution strategy. VULCAN-CFD provides geometric flexibility for structured grid simulations by allowing for arbitrary face-to-face C(0) continuous and non-C(0) continuous block interface connectivities. The unstructured grid paradigm allows for mixed element meshes that contain any combination of tetrahedral, prismatic, pyramidal, and hexahedral cell elements. The VULCAN-CFD flow solver is fully parallelized using MPI (Message Passing Interface) libraries, allowing for efficient simulations on High Performance Computing (HPC) systems. This document provides a description of the physical models available in the software.					
15. SUBJECT TERMS Computational Fluid Dynamics, Aerodynamics, Turbulence, Combustion					
16. SECURITY CLASSIFICATION OF:			17. LIMITATION OF ABSTRACT UU	18. NUMBER OF PAGES 66	19a. NAME OF RESPONSIBLE PERSON STI Information Desk (help@sti.nasa.gov)
a. REPORT U	b. ABSTRACT U	c. THIS PAGE U			19b. TELEPHONE NUMBER (Include area code) (757) 864-9658